# Monte Carlo Simulation of Baryon and Lepton Number Violating Processes at High Energies[1]

**M.J. Gibbs**

Cavendish Laboratory, University of Cambridge
Madingley Road, Cambridge CB3 0HE, U.K.

**A. Ringwald,** [2] **B.R. Webber** [3]

Theory Division, CERN, CH-1211 Geneva 23, Switzerland

and

**J.T. Zadrozny** [4]

Cavendish Laboratory, University of Cambridge
Madingley Road, Cambridge CB3 0HE, U.K.

## Abstract

We report results obtained with the first complete event generator for electroweak baryon and lepton number violating interactions at supercolliders. Typical events contain of the order of 50 electroweak gauge bosons, some Higgs bosons and quarks and leptons of all generations. There is still great uncertainty about the expected rate, but an event generator is needed in any case to establish what experimental limits can be placed on the cross section, and to determine whether, even if such spectacular events are seen, baryon and/or lepton number violation can be conclusively demonstrated. We find that baryon number violation would be very difficult to establish, but lepton number violation can be seen provided at least a few hundred L violating events are available with good electron or muon identification in the energy range 10 GeV to 1 TeV. The event generator, which takes the form of a package (HERBVI) interfacing to the existing simulation program HERWIG, should be useful for the coming period of detailed experiment design for the Large Hadron Collider (LHC) at CERN.

---

[2]Present address: DESY, Hamburg, Germany.
[3]Present address: Cavendish Laboratory, Cambridge, UK.
[4]Present address: 31 Moran Avenue, Princeton, New Jersey, USA.

# 1  Introduction

Current experiments have given us no evidence for physics beyond the Standard Model. Indeed, the Standard Model may be valid, as an effective theory, up to very high energies, say the Planck mass, $10^{19}$ GeV, if the Higgs mass is below several hundreds of GeV. Even this case, however, does not necessarily imply that no new phenomena will be seen in the multi–TeV range which will be explored by future colliders such as the CERN LHC. There is the intriguing possibility that, above a parton–parton centre of mass threshold in the multi–TeV range, the cross section for the nonperturbative production of many, $\mathcal{O}(\alpha_W^{-1})$, weak bosons W(Z) may be observably large. Unfortunately, there is only circumstantial evidence for this to happen which is, to a large extent, just based on the observation that leading order perturbative calculations for the production of $\mathcal{O}(\alpha_W^{-1})$ weak bosons violate unitarity near the threshold of $\mathcal{O}(\alpha_W^{-1} m_W)$ TeV. This happens both for processes with [1–3] and without [4–6] baryon and lepton number violation (BLNV). At present it is an open question whether the *actual* (beyond perturbation theory) multi-W(Z) cross sections become observably large at such multiplicities and energies (for recent reviews see [7–9]). New theoretical methods are needed to answer this important question.

In the meantime one can contemplate the prospects of settling the issue experimentally. Multi-W(Z) processes at the LHC would be clearly distinguishable from any other Standard Model process [10]. This is due to the hadronic and leptonic decays of the W's and Z's, which lead to hundreds of charged hadrons and photons with transverse momenta in the GeV range, and to tens of prompt leptons with transverse momenta in the tens of GeV range. However, the question whether BLNV can be demonstrated in such a multi-particle environment has not been answered conclusively [10, 11]. It is the purpose of this paper to investigate this question.

Using the results of leading–order BLNV calculations, it is possible to create a phenomenological model of these processes, with variable parameters to represent the main sources of theoretical uncertainty. In this paper such a model is postulated, and implemented using a Monte Carlo event generator. The program, which takes the form of a package HERBVI [12] operating within the environment of the HERWIG event generator, also allows the generation of B and L conserving multi–W(Z) events. With this package computer simulations can be performed which permit the feasibility of demonstrating BLNV to be investigated.

The layout of this paper is as follows. In the remainder of this section we describe the theoretical basis of electroweak BLNV. Section 2 is a discussion of our approach to modelling BLNV processes at supercolliders, based on the (rather uncertain) theoretical expectations, and of practical issues that arise in the construction of an event generator. We formulate two contrasting BLNV models, one based on leading-order matrix elements (LOME) and one using a simpler phase-space approach with fixed boson multiplicity. We also discuss the possible backgrounds to BLNV, and how we model the dominant background, which is expected to consist of B and L conserving multi–W(Z) events.

Section 3 contains the results of our Monte Carlo studies. We present results for the simpler model at three energies, including that proposed for the LHC. The LOME model requires a higher energy and so in that case we show results only at 40 TeV. We present our

conclusions in Sect. 4. Brief details of the HERBVI package, used to obtain the majority of the results in Sect. 3, are contained in an appendix.

## 1.1   Instanton-induced B and L violation

Owing to the chiral anomaly [13–15] and the V–A structure of weak interactions, B and L are not strictly conserved in the Standard Model [16, 17]. In the presence of nontrivial SU(2) gauge fields $W_i$, the fermionic quantum numbers change according to

$$\triangle L_e = \triangle L_\mu = \triangle L_\tau = \frac{1}{3}\triangle B = -\triangle N_{\text{CS}}, \tag{1}$$

where

$$N_{\text{CS}} \equiv \frac{\alpha_W}{4\pi} \int d^3x \; \epsilon^{ijk} \; \text{tr}\left( F_{ij}W_k - \frac{2ig}{3}W_iW_jW_k\right) \tag{2}$$

denotes the Chern–Simons number of the gauge field, $F_{ij}$ is the SU(2) field strength, and $\alpha_W \equiv g^2/(4\pi)$ the weak fine structure constant. As is suggested by eqs. (1) and (2), strong, nonperturbative gauge fields, of $\mathcal{O}(g^{-1})$, are needed in order to change the Chern–Simons number, or, equivalently, the fermion numbers, by an integer amount. This is reflected by the fact that there exists, on topological grounds, an energy barrier [18, 19] between gauge fields whose Chern–Simons numbers differ by an integer. The minimum barrier height is given by the energy of a static saddle–point solution, the so called "sphaleron" [20, 21], which depends slightly on the Higgs mass,

$$M_{\text{sp}} = 2 \; B(m_H/m_W) \; \frac{m_W}{\alpha_W} \; \simeq \; 7\text{–}14 \text{ TeV} \; , \tag{3}$$

where the parameter $B$ is restricted to lie in the range $1.57 \leq B \leq 2.72$. At low energies ($\ll M_{\text{sp}}$), therefore, anomalous BLNV processes are only possible by quantum tunnelling under the topological barrier, i.e. the corresponding amplitudes are exponentially suppressed by a tunnelling factor,

$$\mathcal{A}^{\text{BV}}_{E \ll M_{\text{sp}}} \propto \text{e}^{-2\pi/\alpha_W} \sim 10^{-78}, \tag{4}$$

which leads to unobservably small cross sections or decay rates [16, 17].

The amplitude (4) is expected to be enhanced when the process involves a large number of gauge and/or Higgs bosons. Consider the following BLNV process, which might be observable in high-energy proton-proton collisions:

$$q \; + \; q \rightarrow 7 \; \bar{q} \; + \; 3 \; \bar{l} \; + \; n_B \; \text{W(Z)} \; + \; n_H \; \text{H.} \tag{5}$$

The amplitude for this process can be estimated by means of the instanton approach [16,17]. The instanton is a time–dependent tunnelling solution which interpolates between gauge fields whose Chern–Simons numbers differ by one unit and passes through sphaleron–like fields for particular values of its collective coordinates. It was found in refs. [1, 2], by expanding the path integral about the instanton, that, in leading–order ($LO$) in the coupling $\alpha_W$, the amplitudes for the processes (5) grow with multiplicity and parton–parton centre of mass energy $\sqrt{\hat{s}}$ like

$$\mathcal{A}^{\text{BV}}_{n_B,n_H \; LO} \sim (n_B + n_H)! \; \alpha_W^{(n_B+n_H)/2} \; \text{e}^{-2\pi/\alpha_W} \left(\frac{\sqrt{\hat{s}}}{n_B \; m_W}\right)^{n_B} m_W^{-(n_B+n_H)}. \tag{6}$$

2

At high energies, these pointlike S-wave amplitudes violate unitarity. Owing to the facto-rial growth of the amplitudes (6) with the number of produced bosons, this violation of unitarity sets in at multiplicities of $\mathcal{O}(\alpha_W^{-1})$ and at parton-parton centre of mass energies of $\mathcal{O}(\alpha_W^{-1} m_W)$, i.e. the sphaleron energy (3).

The corresponding parton level cross section, $\hat{\sigma}_{LO}$, due to the leading order matrix element (LOME) of instanton-induced BLNV (5), is given by [1, 2]

$$
\begin{aligned}
\hat{\sigma}^{\text{BV}}_{n_B, n_H\ LO} \ = \ & \tilde{C} \mathcal{G}^2 2^n v^{-2n} \left[ \frac{\Gamma\left(n + \frac{103}{12}\right)}{\Gamma\left(\frac{103}{12}\right)} \right]^2 \frac{1}{n_B! n_H!} \\
& \times \int \prod_{i=1}^{10} \frac{\mathrm{d}^3 p_i}{(2\pi)^3 2E_i} E_i \prod_{j=1}^{n_B} \frac{\mathrm{d}^3 p_j}{(2\pi)^3 2E_j} \frac{2\left(4E_j^2 - m_W^2\right)}{m_W^2} \\
& \times \prod_{k=1}^{n_H} \frac{\mathrm{d}^3 p_k}{(2\pi)^3 2E_k} (2\pi)^4 \delta^{(4)} \left( P_{\text{in}} - \sum_{i=1}^{10} p_i - \sum_{j=1}^{n_B} p_j - \sum_{k=1}^{n_H} p_k \right) .
\end{aligned}
\tag{7}
$$

In this expression $n_B$ is the number of vector bosons and $n = n_B + n_H$. The effective coupling constant $\mathcal{G}$ is

$$
\mathcal{G} = 1.6 \times 10^{-101} \ \text{GeV}^{-14},
\tag{8}
$$

$v = 2m_W/g$ is the Higgs field vacuum expectation value, and $\tilde{C}$ is a numerical factor representing the effect of averaging and summing over incoming and outgoing states of the fermions. The leading order result $\hat{\sigma}^{\text{BV}}_{n_B, n_H\ LO}$, taken at the dominant multiplicities, is plotted in Fig. 1. As anticipated, it rises rapidly with centre of mass energy, and violates the S-wave unitarity bound (shown as a dashed line on the same plot)

$$
\hat{\sigma}_{unit}\left(\hat{s}\right) = \frac{16\pi}{\hat{s}}
\tag{9}
$$

at an energy of order the sphaleron energy.

A violation of unitarity is, of course, unacceptable and indicates the importance of higher order corrections. There are strong arguments that the higher order corrections to the fixed multiplicity amplitudes exponentiate in the total cross section of BLNV, such that, to exponential accuracy, the latter can be written as [22–27]:

$$
\hat{\sigma}^{\text{BV}}_{\text{tot}} \equiv \sum_{n_B, n_H} \hat{\sigma}^{\text{BV}}_{n_B, n_H} \propto \exp\left[ \frac{4\pi}{\alpha_W} F\left(\frac{\sqrt{\hat{s}}}{M_0}\right) \right],
\tag{10}
$$

where

$$
M_0 \equiv \sqrt{6}\pi \frac{m_W}{\alpha_W}
\tag{11}
$$

is of the order of the sphaleron mass (3). The exponent itself is known only in a low energy expansion whose first few terms are given by [24, 28–37]

$$
F(\epsilon) = -1 + \frac{9}{8}\epsilon^{4/3} - \frac{9}{16}\epsilon^2 + \mathcal{O}\left(\epsilon^{8/3}\right),
\tag{12}
$$

where $\epsilon \equiv \sqrt{\hat{s}}/M_0$. From this result the following conclusions can be drawn: (i) The total cross section for BLNV, though small, is growing exponentially at $(m_W \ll)\sqrt{\hat{s}} \ll M_0$; in
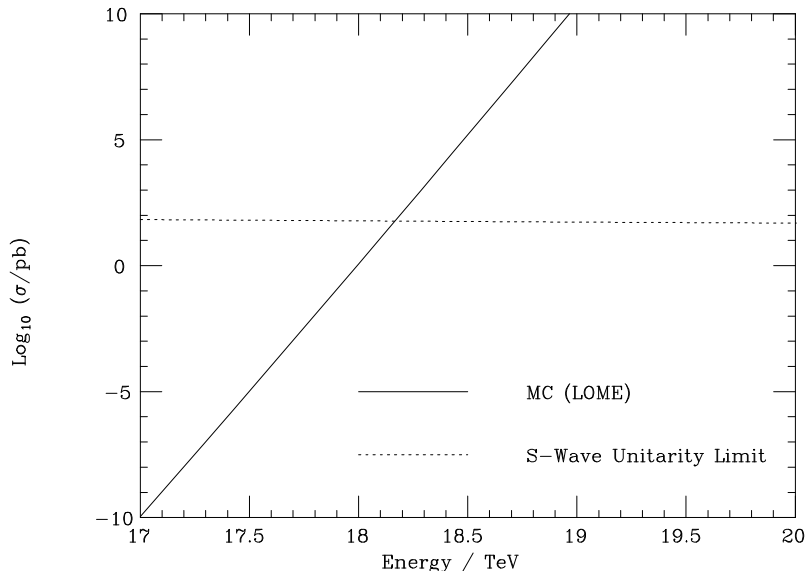
3

Figure 1: Quark-level cross section for leading order BLNV process, solid line. The S-wave unitarity limit is shown as a dotted line.

this energy region, the cross section is insensitive to the Higgs mass. (ii) The different terms in the perturbative expansion of the 'holy grail function' $F$ become comparable in size, and the perturbative expansion breaks down, at $\sqrt{\hat{s}} \sim M_0$.

This breakdown of perturbation theory is not surprising. BLNV processes involve the electroweak gauge fields penetrating the topological barrier between different vacuum sectors. As the energy approaches $M_0$, the height of this barrier, the possibility of crossing the barrier classically arises, and the expansion based upon the instanton tunnelling solution ceases to be valid. Unfortunately, nothing is known about the behaviour of the holy grail function around or above the sphaleron scale. Unitarity arguments [38–40] suggest that its increase will stop at values of order $F \simeq -0.5$, leading to unobservably small cross sections for BLNV. However, this question is not settled finally.

To end this section, we note that at low energies the total cross section (10) is dominated by multi-W(Z) production ($n_B \sim \alpha_W^{-1}$) rather than by multi-Higgs production. In particular one finds at low energies

$$\bar{n}_B \sim \frac{4\pi}{3\alpha_W} \left( \frac{9}{8} \epsilon^{4/3} + \mathcal{O}\left(\epsilon^2\right) \right), \tag{13}$$

whereas

$$\bar{n}_H \sim \frac{4\pi}{\alpha_W} \frac{3}{32} \epsilon^2 \ . \tag{14}$$

## 1.2 Sphaleron decay

It is interesting to compare the above results for the instanton-induced process (5) with those from sphaleron decay. Since the sphaleron lies atop the energy barrier through which tunnelling occurs, it is expected that the lowest energy classical field trajectories which

4

violate B and L will pass (in some sense) close to the sphaleron configuration. Thus, we expect the behaviour of the sphaleron to give us some indication of what should be observed in an actual BLNV event. In particular, the decay products of the sphaleron (which is by nature unstable) should be similar to the gauge and Higgs particle byproducts of a BLNV event. Therefore, one again expects [41, 42] that the dominant BLNV processes will involve $\mathcal{O}(\alpha_W^{-1})$ weak bosons, simply because sphaleron–like intermediate states will typically decay into many W's and Z's.

The decay of the Klinkhamer–Manton sphaleron has been studied numerically in refs. [43, 44]. The sphaleron field configuration was first discretised, and then allowed to evolve under the classical Euler–Lagrange field equations with an imposed condition of spherical symmetry [45–47]. The restriction to spherical symmetry is permissible because the sole decay channel of the Klinkhamer–Manton sphaleron is spherically symmetric [48]; it should be noted, however, that this approach may be used only in the limit of vanishing weak mixing angle $\theta_W$. As a consequence of the imposed spherical symmetry, it is expected that equal numbers of $W^+$, $W^-$ and $Z^0$ of any given polarisation state will be produced after the decay. This is due to the fact that the spherically symmetric ansatz mixes spacetime and group indices, so that particle identities may be interchanged by appropriate spatial rotations.

As a sphaleron decays and the energy carried by the gauge fields moves away from the sphaleron's initial position, the amplitudes of the gauge fields show the $1/r$ attenuation characteristic of spherical radiation. Some time after the sphaleron decay, the amplitudes of the gauge fields become small enough that the nonlinear terms in the gauge field equations of motion are negligible. Thus, a long time after the decay, the various components of the gauge fields behave approximately like free massive fields, and they evolve independently of one another. The multiplicities can then be measured by interpreting the classical fields in terms of coherent states [49–51].

Figure 2 shows the expected particle multiplicities in sphaleron decays for several values of $m_H^2/m_W^2$. The triangles indicate the expected numbers of transversely polarised weak bosons per helicity state and per particle type ($\bar{n}_T$), and the squares show the expected numbers of longitudinally polarised bosons per particle type ($\bar{n}_L$). The crosses show the expected numbers of Higgs bosons ($\bar{n}_H$). The total number of gauge bosons is then

$$\bar{n}_B = 6\bar{n}_T + 3\bar{n}_L \ . \tag{15}$$

The expected number of gauge bosons is seen to vary weakly with the Higgs mass and is of $\mathcal{O}(\alpha_W^{-1})$, as anticipated.

Setting $\sqrt{\hat{s}} = M_{\rm sp}$ leads to

$$\epsilon_{\rm sp} \equiv \frac{M_{\rm sp}}{M_0} = \frac{2}{\sqrt{6}\pi} B(m_H/m_W) \simeq 0.4 \ - \ 0.7 \ , \tag{16}$$

which may be computed readily from the table of $M_{\rm sp}$ versus $m_H$ provided in [21]. Figure 3 compares the expected gauge boson multiplicities computed from (15), shown by triangles, with those given by Eq. (13), denoted by diamonds. It can be seen that the multiplicities predicted by (13) are roughly 30% smaller than those expected from sphaleron decays. This discrepancy is not very surprising in view of the fact that the perturbative expansion of $F(\epsilon)$ does not converge rapidly for values of $\epsilon$ so near to unity.
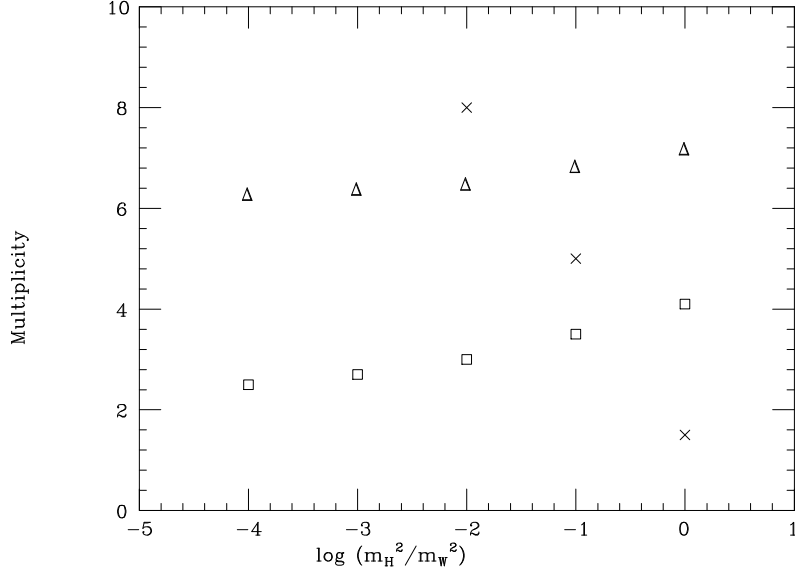
Figure 2: Sphaleron decay products as a function of the Higgs mass. Points shown on this graph show the numbers of each kind of particle in each possible polarisation state: triangles represent transversely polarised gauge bosons, squares show longitudinally polarised bosons, and crosses denote Higgs particles.
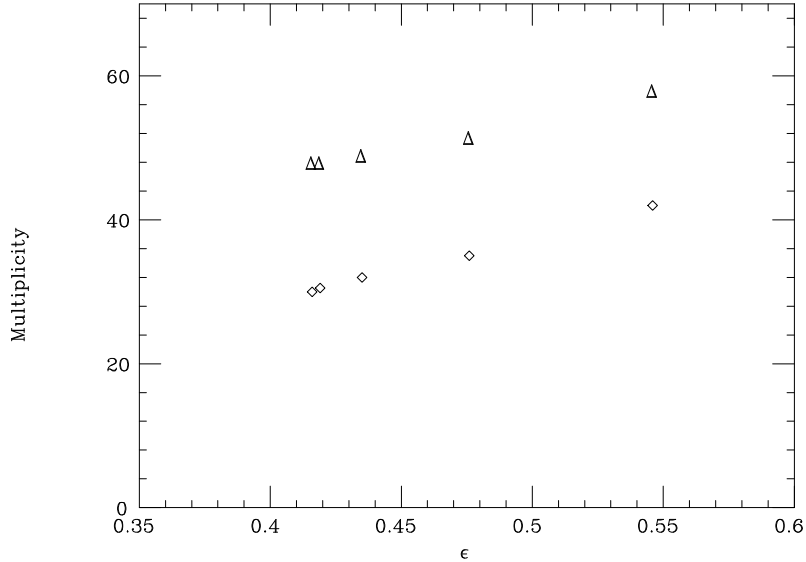


Figure 3: Mean number of gauge bosons, $\bar{n}_B$, expected to be produced in a baryon number–violating event, as a function of $\epsilon = \sqrt{\hat{s}}/M_0$, where $M_0 = \sqrt{6}\pi m_w/\alpha_W$. Triangles show $\bar{n}_{\mathrm{B}}$ from sphaleron decays, and diamonds show $\bar{n}_{\mathrm{B}}$ from Eq. (13).

## 2    Modelling B and L violation

In the absence of a more complete theory at energies of order the sphaleron energy, we will use the gross features of instanton and sphaleron calculations, such as the threshold–like

behaviour of the cross section and the parametrically large vector boson multiplicity, as a guide for phenomenological modelling of electroweak BLNV. The steeply rising cross section means that BLNV processes have a threshold nature. Three parameters are used which encompass the main features of the processes: a threshold energy $\sqrt{\hat{s}_0}$, a threshold cross section $\hat{\sigma}_T$, and the boson multiplicity, $n_B$. The parton level cross section is then modelled as a step function

$$\hat{\sigma}\left(\sqrt{\hat{s}}\right) = \hat{\sigma}_T \, \theta\left(\sqrt{\hat{s}} - \sqrt{\hat{s}_0}\right) \tag{17}$$

following the approach used in [10]. We assume that in the rest frame of the interacting partons the events are isotropic, and that the outgoing particles have an energy distribution that fills the available phase space uniformly. We first discuss the model parameters and general assumptions, and then, in separate subsections, explain the detailed modelling of events and background.

The magnitude of $\hat{\sigma}_T$ is obviously a crucial quantity, as it determines the rate at which the interactions will occur. It is also difficult to estimate because of the theoretical uncertainties, discussed above. For this reason we have performed estimates in terms of the number of events required to verify the existence of BLNV, assuming a comparable background of B and L conserving 'multi–W' events with a similar boson multiplicity. The rationale behind this model for the background is presented in Sect. 2.4.

The high energy processes under consideration mean that, for any $pp$ collider proposed for the near future, the threshold energy $\sqrt{\hat{s}_0}$ is a significant fraction of the total beam energies. Consequently, events will be at large momentum fractions $x$, and also will tend to be central within the detector. The exact size of $\sqrt{\hat{s}_0}$ is not significant for our studies. We have set this parameter at the point where the instanton calculation violates the S-wave unitarity bound, $\sim M_0$, except for the studies performed at 17 TeV where the value of 5 TeV ($\sim 2m_W/\alpha_W$) is used.

Convolution of (17) with the appropriate proton structure functions allows a comparison of the relative rates of processes with similar parton-level cross sections mediated by the possible initial state combinations of $qq$, $q\bar{q}$, and $\bar{q}\bar{q}$ at a $pp$ collider. These relative rates are plotted versus threshold energy in Fig. 4. The results shown were obtained using the EHLQ structure functions for the proton [52], but the dominance of $qq$ processes at high threshold energies is not sensitive to the choice of structure functions. It follows simply from the fact that the valence $u$ and $d$ quark distributions dominate over the sea quarks and gluons at high values of the parton momentum fraction $x$.

For BLNV, which can only occur for incoming $qq$ or $\bar{q}\bar{q}$, the latter contribution is two to three orders of magnitude smaller than the former. Therefore the contribution of BLNV with the opposite sign (creation of baryons as opposed to antibaryons) is negligible.

In this paper, two alternative methods for generating the boson multiplicity $n_B$ are used. One approach is to set $n_B = 30 \sim 1/\alpha_W$ as this is the multiplicity scale at which the violation of unitarity arises [10]. The second approach is to distribute $n_B$ according to the LOME expression (7). In either case, the high multiplicity of electroweak bosons means that Monte Carlo techniques that can generate energy and momentum configurations of many massive particles efficiently have to be used. This is discussed in Sect. 2.1.
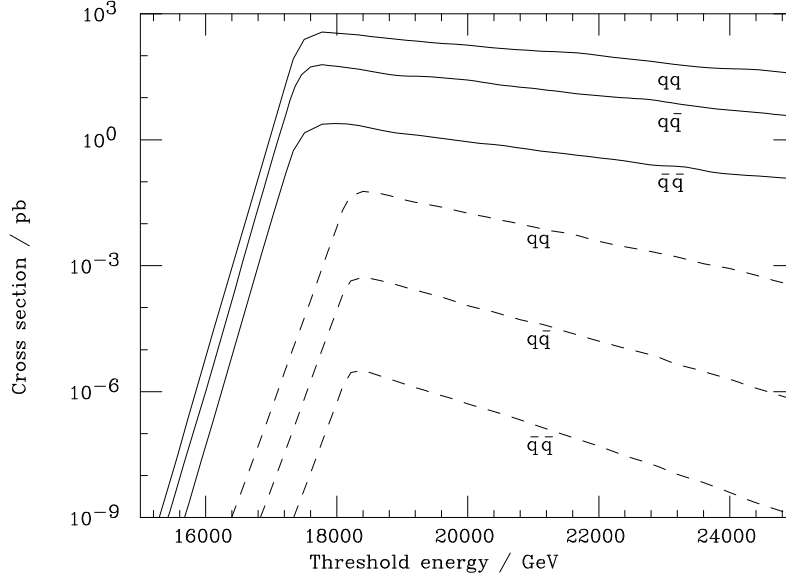
Figure 4: Convolution of step threshold function with proton structure functions for $pp$ energies of 40 TeV (dashed line) and 200 TeV (solid line). The parton level cross section, $\hat{\sigma}_T$, has been taken as the minimum of either the value from the LOME calculation or the S-wave unitarity limit.

We now give a justification of the assumption that particles can be generated isotropically. We saw above that valence quark interactions are dominant. The valence quark structure functions at large $x$ have the approximate form

$$f(x) = (1 - x)^n, \quad n \simeq 3 \tag{18}$$

and the convolution of these structure functions with (17) produces events with $\hat{s} = x_1 x_2 s$ close to the threshold, where higher partial waves are suppressed and so the angular distribution is approximately isotropic.

We can characterize the available energy per particle by a proportionality constant [10]

$$f_W = \frac{\sqrt{\hat{s}}}{M_{tot}}, \tag{19}$$

where

$$M_{tot} = \sum_i m_i \tag{20}$$

is the total mass of the outgoing particles. The average kinetic energy per particle can then be estimated using

$$\bar{E} \sim (f_W - 1)\, \bar{m} \tag{21}$$

for an average particle mass $\bar{m}$. For values of $f_W$ close to one, the average kinetic energy per particle is small, and one can expect that events will be fairly isotropic. This isotropic character will be reduced for large values of $f_W$.

8

## 2.1 Boson final states

Evaluation of the LOME cross section (7) has been performed using a Monte Carlo technique. This approach is closely related to the generation of events for Monte Carlo simulations. Events are generated uniformly in phase space for a fixed particle configuration $(n_B, n_H, \mathcal{C}_f)$, where the symbol $\mathcal{C}_f$ represents the fermion configuration. For each event, a weight that is the product of the matrix element for the event and the phase space integral for the configuration is calculated. The average of these weights is then the Monte Carlo estimate of the cross section.

The phase space integral is calculated using the saddle point method [53]. This method is based upon Laplace transforming the integral in order to remove the delta function, leaving an inverse transform, which can then be evaluated using a saddle point approximation. This technique can also be used to evaluate the cross section (7); whilst this allows computation of the cross section it is restrictive from an event generation point of view.

For a given energy and particle configuration, the generation of events is performed using the MAMBO Monte Carlo algorithm [54]. This algorithm produces configurations in phase space obeying energy and momentum constraints. The algorithm is more efficient than others, such as RAMBO [55] from which it was derived, because various parameters are tuned for each different configuration of particles and total energy. The events generated by MAMBO each have an associated weight $w$. These weights are distributed in the range 0 to 1, and so the correct unweighted distribution is obtained by rejecting events with $w$ less than a random number generated in this range.

The evaluation of the matrix element for each event is the third step in the cross section calculation. Computation of the factor in (7) for each gauge boson, averaging over the set of generated events, and multiplying by the phase space integral for the particle configuration, gives us an estimate of the leading-order cross section $\hat{\sigma}_{LO}(n_B, n_H, \mathcal{C}_f)$ for a given set of final state particles. The total quark level cross section is then obtained by summing over all possible particle configurations. The particle numbers are constrained by the requirement that the total mass of all the outgoing particles has to be less than the energy of the interaction.

In summing over the number of vector bosons, the relative number of $Z^0$ bosons and photons has to be considered [56]. The instanton is a field configuration in unbroken SU(2) gauge theory; in the standard model this symmetry is broken to give the physical particles $W^\pm$, $Z^0$ and $\gamma$. Whilst equal numbers of $W^+$, $W^-$ and $W^0$ bosons of the unbroken symmetry are produced by the instanton interaction, the $W^0$ bosons are projected onto the $Z^0$ and $\gamma$ physical states, with the relative probabilities of $\cos^2\theta_W$ and $\sin^2\theta_W$ respectively. The probability distribution for $n_\gamma$ photons and $n_Z$ $Z^0$ bosons is then described by a binomial distribution.

This procedure also yields the mean boson multiplicity $\bar{n}_B$ as a function of energy, as

$$\bar{n}_B = \frac{\sum_{n_B} n_B \hat{\sigma}_{LO}(n_B, \mathcal{C}_f)}{\sum_{n_B} \hat{\sigma}_{LO}(n_B, \mathcal{C}_f)}. \tag{22}$$

A plot of $\bar{n}_B$ is shown in Fig. 5, along with the estimate from the 'holy grail' function $F$,
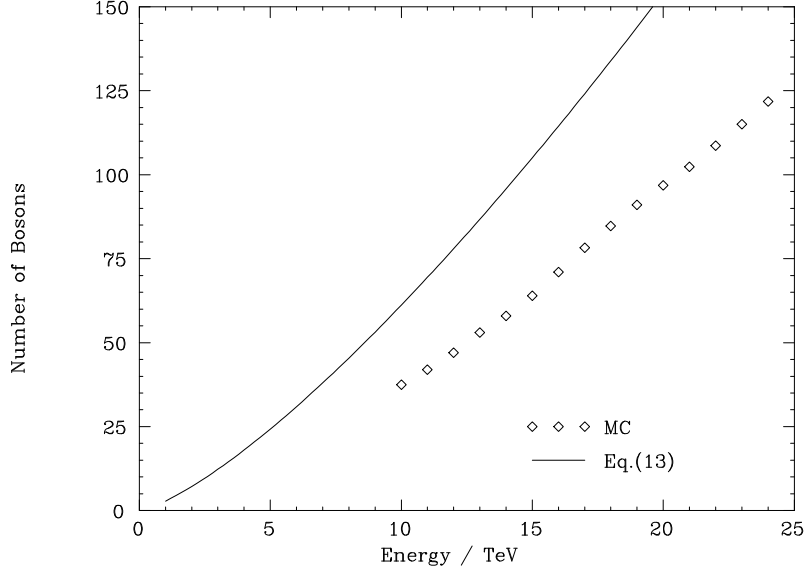
Figure 5: Mean number of bosons as a function of energy. Diamonds LOME prediction, solid line Eq. (13).

which is shown as a solid line on the same plot. The difference is due to the reduced phase space available when one considers massive electroweak bosons.

At a given multiplicity $n_B$, integration over all possible SU(2) configurations of the instanton produces a non-trivial momentum structure in the final state, as noted by Espinosa [2]. This structure contains terms of the form $(p.q)$ and $(\epsilon_{\mu\nu\alpha\beta}p_\mu q_\nu k_\alpha l_\beta)$, where $p$, $q$, $k$ and $l$ are particle momenta and polarisation vectors. The large number of particles from the instanton interaction means that there will be many $(\sim [4n_G + 2n_B + n_H - 1]!!)^5$ such terms [56]. Whilst calculation of all these terms is not feasible, it is reasonable to assume that their overall effect will be to produce an approximately uniform distribution in solid angle. However, these terms could modify the energy spectra of the outgoing particles. For example, the LOME expression (7) was obtained without performing any SU(2) averaging, and in this case the bosons each have a factor of $(4E^2 - m_W^2)/m_W^2$. This factor favours configurations with higher boson energy. Such a factor has not been included in the simulations when either the $n_B = 1/\alpha_W$ or LOME prescriptions were used.

The averaging over SU(2) configurations also requires that the number of Higgs bosons involved in the interaction is even. This can be identified with the observation that the integration over all SU(2) configurations of an odd number of rotation matrices is identically zero. Recall that the number of Higgs particles $\bar{n}_H$ is expected to be small from (14). We model the number of Higgs particles at a given boson multiplicity $n_B$ using the relative sizes of the LOME estimate (7) as a function of $n_H$.

---

[5]We use the double factorial notation, whereby $n!! = n(n-2)(n-4)...3.1$ for odd $n$.

## 2.2 Fermion final states

The structure of instanton-induced BLNV involves three quarks and a lepton from each fermion generation. This structure arises because the instanton determinant includes a zero mode for each fermion doublet; there is a quark doublet for each of the three colours of QCD. The integral over all SU(2) configurations ensures overall charge conservation, and any difference in total charge between the incoming and outgoing fermions is balanced by the relative numbers of charged bosons.

In order to generate the fermion configuration, one member of each doublet has to be included in the interaction. The incoming quarks from the protons determine two of the three quark doublets for the lightest generation, leaving the other seven antiquark and three antilepton doublets to be chosen.

Our simulations use a simple phase space model to perform the fermion selections. The calculation of the phase space for $n$ particles, $V_n(s)$, by the saddle point method leads, via a Laplace transform, to the expression

$$V_n(s) = \frac{1}{4\pi^2 i \sqrt{s}} \int_{c-i\infty}^{c+i\infty} d\beta \, \beta^2 I_1 \left(\beta\sqrt{s}\right) \Phi\left(\beta\right) \tag{23}$$

where

$$\Phi\left(\beta\right) = \prod_{i=1}^{n} \phi_i\left(\beta\right) \tag{24}$$

is the product of the individual contributions of each particle to the overall phase space, and $I_1$ is the entire modified Bessel function. The value of $c$ is chosen so that all singularities of the integrand lie to the left of the contour in the complex $\beta$ plane. The contribution of a particle of mass $m_i$ is

$$\phi_i = \frac{2\pi m_i}{\beta} K_1\left(m_i\beta\right) \tag{25}$$

where $K_1$ is the singular modified Bessel function, and in the massless case is simply

$$\phi_i = \frac{2\pi}{\beta^2} \ . \tag{26}$$

The integral (23) can be performed in the saddle point approximation. Note that the limiting values of the saddle point, $\bar{\beta}$, for the cases of all $n$ particles in the extreme relativistic and non-relativistic limits are

$$\begin{aligned}
\bar{\beta}_{ER} &= \frac{2n - 3/2}{\sqrt{s}} \ , \\
\bar{\beta}_{NR} &= \frac{3}{2} \frac{(n-1)}{\sqrt{s} - \Sigma m_i}
\end{aligned} \tag{27}$$

respectively.

Neglecting the effect on $\bar{\beta}$ of choosing between two particles in a doublet with different masses, we can estimate the relative probability of picking a particle of mass $m_1$ as opposed
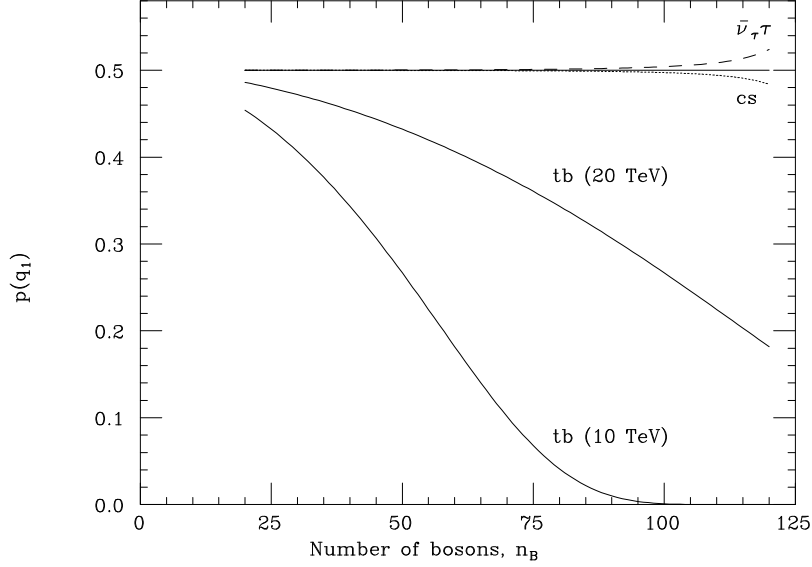
Figure 6: Relative probability of emission for fermion doublets. Energy $= 20$ TeV except for the lower $tb$ line.

to one of mass $m_2$ as

$$
\begin{aligned}
p &= \frac{\phi_1}{\phi_1 + \phi_2} \\
&= \left( 1 + \frac{m_2 K_1 \left( m_2 \bar{\beta} \right)}{m_1 K_1 \left( m_1 \bar{\beta} \right)} \right)^{-1}
\end{aligned}
\tag{28}
$$

for two massive particles, and by

$$
p = \left( 1 + m_2 \bar{\beta} K_1 \left( m_2 \bar{\beta} \right) \right)^{-1}
\tag{29}
$$

for a doublet with $m_1 = 0$.

We find that, with the exception of the $\bar{t}\bar{b}$ doublet, the effect of mass on the probability $p$ is negligible. For the heavy quark case, the relative probability of $\bar{t}$ compared to $\bar{b}$ production is reduced as the boson multiplicity increases, as shown in Fig. 6. It is evident that the only significant effect occurs at large boson multiplicity, where the phase space is sensitive to mass effects.

The fermion configurations are described in terms of the gauge eigenstates of the electroweak theory. It is the mass eigenstates of the quark fields that are observed, and the gauge eigenstates of the $I_3^W = -\frac{1}{2}$ quarks have to be projected onto the mass ones. The states are related by the CKM matrix $U$ by

$$
|\text{mass}\rangle = U |\text{gauge}\rangle .
\tag{30}
$$

12

## 2.3 Hadronisation of B violating final states

The objective of a Monte Carlo event generator is to generate complete final states in all the detail that could in principle be observed by a perfect detector. In the case of colourless produced particles (electroweak and Higgs bosons, and leptons) it is a reasonable approximation to suppose that they interact with the detector or decay independently, apart from possible spin correlations that have not yet been computed but are probably of secondary importance. For coloured particles (quarks and gluons), however, we know that confinement plays a rôle that cannot be neglected, giving rise to hadronic jets whose properties are only indirectly related to those of the primary partons. One of the main successes of modern event generators [57–60] has been the surprisingly accurate representation of jet properties that they give when applied to conventional processes such as $e^+e^-$ annihilation. It is therefore natural to take over the detailed machinery of jet fragmentation in such generators and apply it, unchanged as far as possible, to the unconventional process of baryon number violation.

According to the viewpoint adopted in all the widely-used QCD event generators, the process of jet production and fragmentation takes place in three distinct phases. First, on the very shortest relevant timescale (the electroweak scale in this case), quasi-free partons are produced with the distributions prescribed by the hard process matrix elements. Next, these primary partons give rise to *parton showers* via successive gluon bremsstrahlung and, less commonly, quark-antiquark pair production. The showers can be followed perturbatively until the timescale approaches the hadronic scale $1/\Lambda_{\mathrm{QCD}}$, when the running QCD coupling $\alpha_s$ becomes large. At this stage the shower development is terminated by imposing a parton virtuality cutoff $Q_0 > \Lambda_{\mathrm{QCD}}$.

The final phase of jet fragmentation, in which the showers at the cutoff scale $Q_0$ are converted into hadrons, is called *hadronization*. This process is not well understood at a fundamental level but various models have been developed which can describe it in some detail. In the HERWIG Monte Carlo program [57, 58], a cluster model [61] is used: all remaining gluons in the showers are split non-perturbatively into quark-antiquark pairs and colourless mesonic clusters form in the resulting cloud of quarks and antiquarks. The observed hadrons come from cluster decay according to a simple phase-space model. In the JETSET program [59, 60] a string model [62] is used: instead of clusters, more extended colour-singlet objects called strings are formed and these fragment sequentially into hadrons.

In the generation of the parton showers, and also for the formation of clusters or strings during hadronization, it is essential to keep track of the colour structure of the process, at least to leading order in $1/N$ where $N$ is the number of colours. An effect of special importance is the colour coherence of soft gluon emission by the primary partons, which sets the limits on parton showering via angular ordering [63, 64]. We first review how this works for conventional baryon-number conserving processes,[6] and then show how it applies equally well in the presence of baryon number violation.

Consider for example the diagram in Fig. 7a, representing a contribution to the ma-

---

[6]For a more extensive review, see for example Ref. [65].
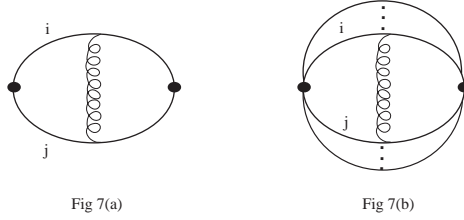
Fig 7(a)          Fig 7(b)

Figure 7: Soft gluon coherence: (a) emission from a $q\bar{q}$ pair, (b) emission contribution from two quarks after a BLNV event.

trix element squared for emission of a gluon of momentum $q$ from a colour-singlet quark-antiquark pair $ij$. In Feynman gauge (neglecting quark masses) this is the only contribution, and in the soft limit it gives a spin- and colour-averaged emission probability of the form

$$
\begin{aligned}
dP_{ij} &= \frac{g^2}{N}\mathrm{Tr}(t^a t^a)\frac{p_i \cdot p_j}{p_i \cdot q \; p_j \cdot q}\frac{d^3 q}{2(2\pi)^3 q} \\
&= C_F \frac{\alpha_s}{\pi}\frac{dq}{q}\frac{d\Omega}{4\pi}W_{ij}
\end{aligned} \tag{31}
$$

where $t^a$ are the colour matrices in the fundamental representation, $C_F = \mathrm{Tr}(t^a t^a)/N = (N^2-1)/2N$ and the radiation function $W_{ij}$ is given by

$$
W_{ij} = \frac{(1-\cos\theta_{ij})}{(1-\cos\theta_i)(1-\cos\theta_j)} \equiv \frac{\xi_{ij}}{\xi_i \xi_j}\;, \tag{32}
$$

$\theta_{ij}$ being the angle between lines $i$ and $j$ and $\theta_i$ $(\theta_j)$ the angle of emission of the gluon with respect to line $i$ $(j)$.

The way in which the radiation function (32) leads to angular ordering can be seen as follows. We write

$$
W_{ij} = W_{ij}^i + W_{ij}^j \tag{33}
$$

where

$$
W_{ij}^i = \frac{1}{2\xi_i}\left(1 + \frac{\xi_{ij}-\xi_i}{\xi_j}\right) \;. \tag{34}
$$

Then $W_{ij}^i$ and $W_{ij}^j$ contain the leading collinear singularity as $\theta_i \to 0$ and $\theta_j \to 0$ respectively. Furthermore if we average $W_{ij}^i$ over $\phi_i$, the azimuthal angle of emission with respect to line $i$, we find precisely

$$
\left\langle W_{ij}^i \right\rangle_{\phi_i} = \frac{1}{\xi_i}\Theta(\xi_{ij}-\xi_i) \;. \tag{35}
$$

That is, after azimuthal averaging, $W_{ij}^i$ represents emission inside a cone centred on line $i$ with half-angle $\theta_{ij}$. Similarly $W_{ij}^j$ represents emission in a cone centred on line $j$ with the

14

same half-angle. Outside these cones, the radiation averages to zero, which is what is meant by angular ordering. In the 'coherent parton shower' approximation used in Monte Carlo simulations [66], the radiation function is set equal to zero outside the angular-ordered region. This gives the correct results for quantities that are azimuthally averaged, such as multiplicity and energy distributions. The approximation is also found in practice to be quite accurate for global quantities that are in principle sensitive to azimuths, such as event shapes, because the contributions from angular-disordered regions tend to cancel and are in any case numerically small, such regions being far from all collinear singularities. A similar analysis can be performed for soft gluon emission from heavy quark systems: here the collinear singularities are screened but angular-ordered regions are still enhanced [67].

The extension of the above treatment to baryon-number violating processes poses no special problems since colour, together with other generators of local gauge symmetries, remains absolutely conserved in the hard process. We consider the soft gluon emission contribution in which the gluon connects lines $i$ and $j$ emerging from a baryon-number violating vertex, Fig. 7b. For $N$ colours, the vertex couples $N$ quarks via the invariant tensor $\epsilon_{ijk...}$. The emission probability becomes

$$dP_{ij} = C_B \frac{\alpha_s}{\pi} \frac{dq}{q} \frac{d\Omega}{4\pi} W_{ij} \tag{36}$$

where the colour factor is

$$C_B = -\frac{\epsilon_{ijk...}\epsilon_{i'j'k...}t^a_{ii'}t^a_{jj'}}{\epsilon_{ijk...}\epsilon_{ijk...}} = \frac{\text{Tr}(t^a t^a)}{N(N-1)} = \frac{C_F}{N-1} \; . \tag{37}$$

If we now make the decomposition (33) of the radiation function, we see that the full contribution with the leading collinear singularity along the direction of line $i$ is given by Eq. (31) with the replacement

$$W_{ij} \rightarrow \frac{1}{N-1} \sum_{j \neq i} W^i_{ij} \; . \tag{38}$$

That is, we should simply average the contribution with respect to all other lines emerging from (or entering) the same baryon-number violating vertex. In the coherent parton shower approximation, this means that we should choose the cone which limits emission from line $i$ to have half-angle $\theta_{ij}$ where $j$ is chosen at random from all other lines at the same vertex. Within this approximation, the parton showers from each line then develop independently.

As already mentioned, in the cluster hadronization model adopted in the HERWIG program [57] all gluons remaining at the end of parton showering are split into quark-antiquark pairs. Colour singlet $q\bar{q}$ combinations are then used to build clusters. This is actually done in the leading-$1/N$ approximation, which greatly simplifies matters since each external colour line in any diagram is then uniquely connected to an external anticolour line with which it forms a singlet. A similar approximation is used in JETSET [59,60] to decide which quarks and gluons should be connected by string segments. For baryon-number violating processes essentially the same procedure can be adopted: all connected external colour-anticolour pairs are first used to form singlet mesonic clusters or strings, leaving sets of $N$ colour or anticolour lines connected to each other via the same hard vertex, which

form singlet baryonic or antibaryonic clusters/strings. Any excess baryons or antibaryons naturally appear amongst the decay products of the latter.

It follows from the above hadronization mechanism that the excess baryons in a B-violating final state tend to be amongst the lower -momentum jet fragmentation products, rather than the leading particles which carry the bulk of the jet momentum. An excess baryon can be a leading particle only if the corresponding excess quark does not emit any gluons above the hadronization cutoff $Q_0$. The probability of this is suppressed by a Sudakov form factor, which decreases faster than any inverse power of the hard process scale.

## 2.4   Backgrounds to B and L violating processes

We consider three possible backgrounds to BLNV processes: non-perturbative multi–W(Z) production, multiple electroweak boson production by perturbative standard model processes, and QCD multijet production.

Non-perturbative multi–W production is expected to occur at high multiplicities, $n_B \sim 1/\alpha_W$, with an energy scale $\sim m_W/\alpha_W$. A detailed discussion, based on the argument that at high energies electroweak theory has a large, essentially constant total inelastic cross section, may be found in ref. [10]. The fermion structure for multi-W production without BLNV is

$$q_1 \; + \; q_2 \to \; q_3 \; + \; q_4 \; + \; n_B \; W(Z) \; + \; n_H \; H, \tag{39}$$

giving a signature similar to the BLNV case considered previously (5), without the primary fermions. It is expected that these processes will have a similar threshold behaviour and cross section to the BLNV ones. We have therefore modelled this background in the same manner as the BLNV signal. In principle, there are also processes initiated by initial-state antiquarks, but again, because of the high threshold the $qq$ combination dominates (see Fig. 4). For simplicity, we exclude the other incoming combinations, as in the BLNV case.

Perturbative multiple production of electroweak bosons by standard model processes has been estimated in refs. [68, 69]. The dominant mechanism is expected to be multiple top quark production: each $t$ decays into a $W$ boson and a $b$-quark jet. At 40 TeV energy the expected $t\bar{t}$ cross section is $3 \times 10^6$ fb while that for $t\bar{t}t\bar{t}$ is expected to be about 400 fb. In contrast, the predicted direct $4W$ cross section is only around 6 fb, which is comparable to the rate via Higgs bosons decaying into $WW$. Clearly, in order for the production of much larger numbers of $W$ bosons to be observable, a breakdown of perturbation theory is required, as assumed above.

Even though each jet from $W$ decay is in principle well defined, for high $W$ multiplicities the number of possible dijet combinations becomes too high for the $W$'s to be reconstructed. At very high multiplicities, the jets will be too close together to be resolved. A typical jet cone size, R[7], of 0.7 means that within a rapidity limit of $|\eta| < 3$ only $12\pi/(\pi 0.7^2) = 24$ jets can be accommodated without overlapping. Thus, for hadronic $W$ decays, we have to

---

[7] $R$ is defined as $R = \sqrt{\Delta\eta^2 \; + \; \Delta\phi^2}$, $\eta = -\ln \tan\theta/2$ is the pseudorapidity and $\phi$ is the azimuth, both with respect to the beam direction.

worry also about pure QCD multi-jet background.

Perturbative QCD multi-jet production has been studied most in the process of $W + n$ jet hadroproduction [70, 71], since this is an important background for top quark searches. The predicted $W + 2$ jet cross section at 40 TeV for jet $p_T > 50$ GeV, $\Delta R_{jj} > 0.7$ and $|\eta_j| < 3$ is about $2 \times 10^6$ fb. Tree-graph calculations for 3 and 4 jets suggest a fall in the cross section by a factor of 2-3 for each additional jet, as long as phase space limitations can be neglected.

QCD multi-jet production without any direct $W$ boson has been less studied. For the same cuts as above, the predicted 2-jet cross section is about $4 \times 10^{10}$ fb. Four and six jet production can be estimated from ref. [72] at roughly $4 \times 10^8$ and $4 \times 10^6$ fb, suggesting a fall of around a factor of 10 for each additional jet. However, these estimates are based on multi-gluon amplitudes, and the $W + n$ jet studies suggest that multi-quark amplitudes play a significant role at high multiplicities. This may explain the smaller rate of decrease seen in those studies. The Monte Carlo estimates of ref. [73] are indeed somewhat higher, but this may be due to a jet definition in terms of invariant mass, $m_{jj} > 6$ GeV, which corresponds to a very narrow $\Delta R_{jj} > 0.1$ at $p_T = 50$ GeV. A fall by a factor between 2 and 10 per additional jet would imply, for example, a perturbative 30 jet cross section of $10^{-9 \pm 9}$ fb.

In a recent paper [74], approximate expressions for high-order multigluon tree amplitudes are used to derive the following estimate for the QCD $n$-jet cross section

$$\sigma_n \sim \frac{1}{s} [z(n, \Delta)]^{n-2} \tag{40}$$

where $s$ is the hard scattering energy scale and $\Delta = m_{jj,min}^2/s$. For $\ln(1/\Delta) \gg n$, the suppression factor $z(n, \Delta)$ has the form

$$z(n, \Delta) \sim \frac{N_c \alpha_S}{2\pi\sqrt{12}} \ln^2(1/\Delta) \tag{41}$$

For the jet definitions used above, taking $\sqrt{s} \sim 10$ TeV gives $\ln(1/\Delta) \gtrsim 10$ and $z > 1$. Thus the approach of ref. [74] implies a breakdown of QCD perturbation theory. Indeed, the instanton approach adopted here for electroweak physics suggests that in QCD such a breakdown would be expected for $n \sim 1/\alpha_s$, with an energy scale of $\Lambda_{\mathrm{QCD}}/\alpha_s$ [10].

For studies of lepton number violation, the lepton content of the background is relevant. Multi–W production and decay would yield many hard charged leptons (about 0.25 per $W$) which would be confused with those from the primary process. In QCD multijet production, from Monte Carlo studies of 2-jet events with jet $p_T > 50$ GeV at 40 TeV, the predicted number of charged leptons per jet was found to be 0.07, mostly from charm decay. Thus 30 jets would provide only 2 charged leptons on average, and these would mostly appear at low transverse momentum.

In conclusion, the cross sections for backgrounds to BLNV are as uncertain as that for the signal. However, if a signal exists, then B and L conserving multi–W processes are likely to occur at a similar rate, and constitute the background most difficult to distinguish from the signal. Consequently we shall concentrate on this background in the Monte Carlo studies in the next section.

| Simulations performed | | | | |
|---|---|---|---|---|
| Energy (TeV) | $n_B$ estimate | $\sqrt{\hat{s}_0}$ (TeV) | $f_W$ | $\bar{E}$ |
| 17 | $1/\alpha_W$ | 5 | 1.8 | 60 |
| 40 (a) | $1/\alpha_W$ | 18 | 7.4 | 450 |
| 40 (b) | LOME | 18 | 2.0 | 80 |
| 200 | $1/\alpha_W$ | 18 | 9.3 | 580 |

Table 1: Monte Carlo simulations performed. All simulations contained a $10^4$ event sample.

# 3  Monte Carlo results

In this section we describe the results obtained by performing Monte Carlo simulations of BLNV processes. The events under consideration are very distinctive, owing to the high number of particles involved. In particular, the large number of leptons present and the high total transverse energy $E_T$ will be useful experimental criteria for isolating multi–W and BLNV events.

Four cases were studied to investigate the observability of B and/or L violation. The configurations of the parameters $n_B$ and $\sqrt{\hat{s}_0}$ used are listed in Table 1, along with approximate values for the energy fraction $f_W$ and the mean energy given by $\bar{E}$. This range of $f_W$ and $n_B$ allows useful comparisons to be made. The simulations were performed using an event generator, HERBVI [12], which incorporates the parametrizations and assumptions described in the previous section. HERBVI is a package designed as an extension to the Monte Carlo program HERWIG, which performs the hadronisation of the final state as described in Sect. 2.3. Some further details are given in the appendix.

The lack of more detailed knowledge of the matrix element means that we have concentrated on the gross properties of the events, such as the excess of antileptons over leptons, as opposed to detailed analysis of momentum spectra or rapidity distributions. In each of the four cases studied $10^4$ simulated events were generated, with $m_{top} = 140$ GeV and $m_{Higgs} = 300$ GeV.

In order to assess the detectability of BLNV, we have conceived a hypothetical detector loosely based on the proposals for detectors at the LHC [75, 76]. The simulations were performed with the following acceptance criteria:

- A minimum of four identified charged leptons of the same family ($e$ or $\mu$) for an event to be accepted

- Pseudo–rapidity coverage up to $|\eta| = 3$

- Minimum particle transverse momentum $p_t$ of 10 GeV

- Electron and muon identification efficiency 95%.

In addition, we define isolated leptons and photons in the same way as the ATLAS LHC
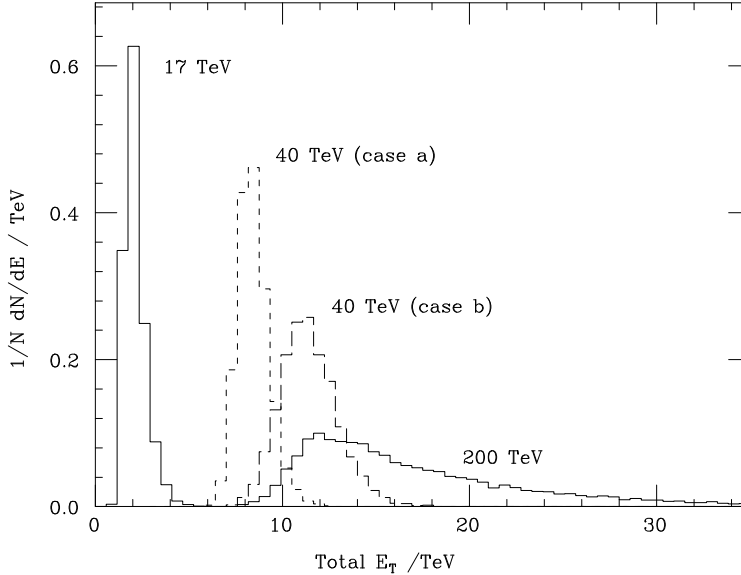
Figure 8: Total transverse energy distribution.

detector proposal [75]. A particle is considered to be isolated if there is a total of less than 12 GeV energy deposited in the detector calorimetery around it within a radius $R < 0.2$.

No cut on $E_T$ has been made in the simulations. In Fig. 8 the distribution of $E_T$ for the four simulations has been plotted. Here $E_T$ is defined as the sum of transverse energy $(m^2 + p_T^2)^{1/2}$ for all *detected* particles. A minimum $E_T$ of 5 TeV ( 1 TeV for the 17 TeV simulation) will include all the events generated here, yet reject virtually all other types of events. Obviously, this cut would have to be 'tuned' in an experimental analysis, but combined with the multiple lepton cut the background from any non–multi–W standard model process should be essentially zero.

## 3.1   Boson Spectra

With the possible exception of photons, the study of bosons from instanton-induced processes will be difficult. It may be possible to reconstruct the leptonic decays of $Z^0$'s; for $W^\pm$ decays this will not be possible due to the large missing momentum from the neutrinos. The identification of jets, and hence the reconstruction of hadronic $W^\pm$ and $Z^0$ and decays, will also be difficult because of the large number of overlapping jets. However, the energy spectra of the bosons produced in the initial interaction are an important aspect of the process since they reflect the characteristic size of the interaction region $\sim 1/m_W$.

The boson energy spectra for the simulations are plotted in Fig. 9. The distributions have been weighted so that the total area under each graph is equal to the average number of each type of boson produced in the interaction, with the exception of the Higgs boson results which have been increased by an factor of ten. The much lower average boson energy of the $f_W \sim 2$ simulations compared to the other two can clearly be seen.

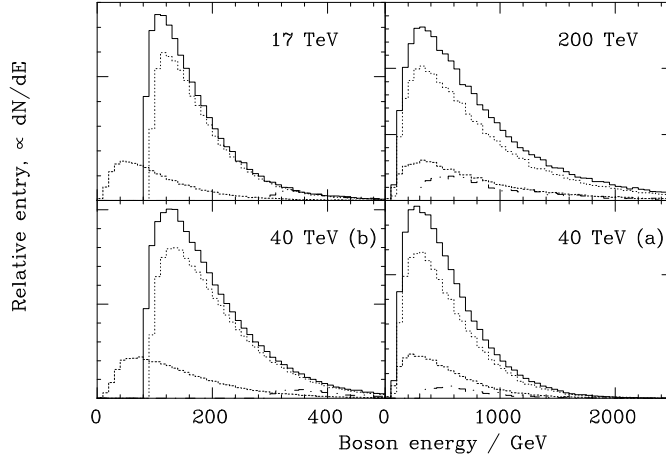The $W^\pm$ distributions from these plots are shown again in Fig. 10 along with the

19

Figure 9: Boson energy spectra. Area under each curve is the average number of bosons by type per event. Solid $W^{\pm}$, dotted $Z^0$, dashed photons, dot-dashed Higgs ($\times 10$).
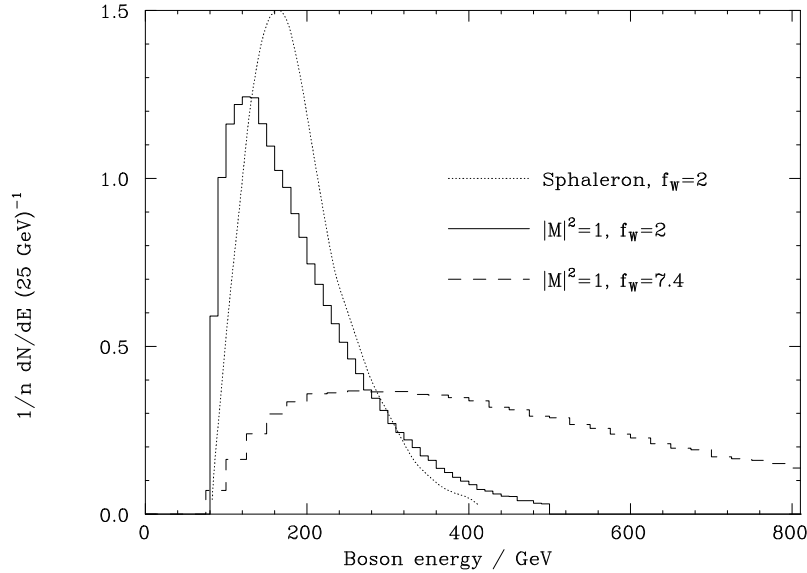


Figure 10: Comparison of boson energy spectra with sphaleron decay spectrum.

sphaleron decay spectra [44] for comparison. The sphaleron decay corresponds to $f_W = 2$. It can be seen that the distribution differs slightly from that of the $f_W = 2$ simulation. The calculation of the sphaleron decay products involves the solving of the non-linear field equations. Therefore the spectra of the outgoing particles from this decay include the effects of final state corrections (but not of the integration over orientations of the classical background field). The similarity of the curves shows that the assumption of a flat distribution of outgoing particles in phase space is a reasonable first approximation. Note however that this assumption yields more particles in the high momentum tail of the distribution.

Direct photons from the primary interaction, which have not been considered before, may provide the best opportunity to investigate the bosonic spectra of the instanton in-
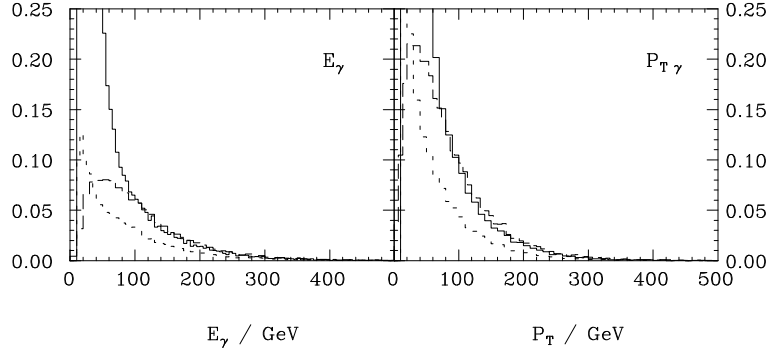
Figure 11: Photon energy spectra for the 17 TeV simulation. Solid line all photons, dashed photons from primary interaction, short-dashed isolated photons.
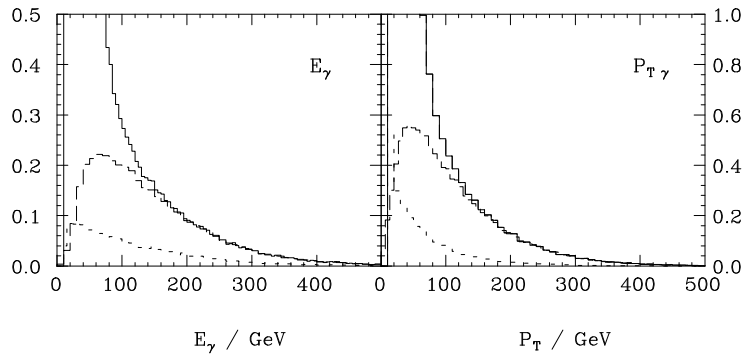


Figure 12: Photon energy spectra for the 40 TeV simulation, using the leading order matrix element estimate for $n_B$. Solid line all photons, dashed photons from primary interaction, short-dashed isolated photons.

teraction. In Fig. 11 the photon $E$ and $p_t$ spectra from the 17 TeV simulation are plotted. Typically $\sim 60$ photons are produced per event, the majority of which are from pion decay and at the low end of the energy spectrum. The tails of the distributions largely comprise direct photons from the primary interaction. The average number of photons produced in this way is $n_B \sin^2 \theta_W / 3$, which corresponds to $\sim 2.2$ for the $n_B \sim 1/\alpha_W$ and $\sim 7.7$ for the LOME estimate respectively. The short-dashed line is the spectrum of photons after the isolation cut had been imposed. For this simulation, the domination of the photon spectra by primary photons for $E > 100$ GeV and $p_t > 100$ GeV means that measurement of photons in this region would provide information on the BLNV process structure. Similar conclusions can be drawn from the other two $n_B \sim 1/\alpha_W$ cases, but in the 40 TeV simulation using the LOME $n_B$ estimate, shown in Fig. 12, there are very few isolated photons. This is because of the larger number of particles in the detector, which makes finding an isolated particle less likely.

The isolation cut removes the lower energy particles, leaving the tails which are mainly composed of photons from the primary interaction. The study of these tails will provide useful information about the underlying process. Any structure from the matrix element of the instanton process will show up in this part of the spectrum. Therefore measurements of photon spectra will be important in any experimental study of BLNV or multi–W phenomena in general. Good calorimetry, especially if a 'tighter' definition of isolation is
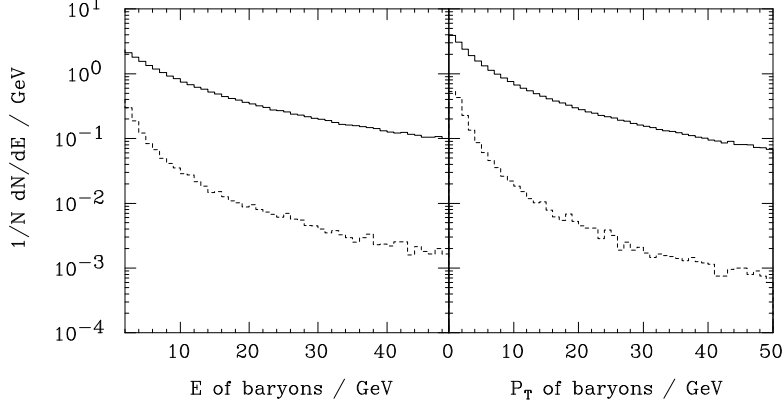
21

Figure 13: Energy and transverse momentum spectra for baryons and antibaryons. Solid line, all baryons and antibaryons, dashed antibaryons from BLNV vertex only.

possible, would aid this task considerably.

## 3.2 Baryon number violation

The high energy threshold of the BLNV processes we are studying, along with the 'central' nature of the events, means that the events are characterised by a large number of particles, $\mathcal{O}\left(\infty r^{\ni-\triangle}\right)$, within the detector. Nevertheless, many final state particles escape detection, either because they do not enter the solid angle covered by the detector, or because their energies are so low that they cannot be reliably detected. Consequently, any verification of BLNV will have to concentrate on averaging quantum numbers over a number of events, with the aim of demonstrating an asymmetry. We therefore focus our analysis on determining quantities that can be used to demonstrate such asymmetries, and on the number of events that will be required.

The large number of particles present in the detector makes the identification of baryons difficult. This is particularly true for any identification technique based upon the reconstruction of the masses of unstable baryons. Furthermore, the excess antibaryons from the BLNV process are at low energies and transverse momentum, as can be seen in Fig. 13. The task of separating these antibaryons from the others produced in the interaction is effectively impossible.

We may demonstrate the difficulty of verifying B violation by making an estimate of the number of events required for observing B violation with a 95% ($3\sigma$) confidence level, assuming for the moment perfect baryon identification within the detector solid angle. We define the baryon number difference $D_B$ as

$$D_B = N_B - N_{\bar{B}} \tag{42}$$

where $N_B$ is the number of detected baryons in a given event, and $N_{\bar{B}}$ the corresponding number of antibaryons. The averaging is performed separately for BLNV and multi-W events. For the 40 TeV /BLNV/ simulation using the LOME estimate for $n_B$, the distributions of $N_B$ and $N_{\bar{B}}$ are plotted in Fig. 14. The means of these distributions are given in

| Baryon number results | | |
|---|---|---|
| Measurement | BLNV | Multi–W |
| $N_B$ | 15.7±0.04 | 15.8±0.04 |
| $N_{\bar{B}}$ | 16.0±0.04 | 15.7±0.04 |
| $D_B$ | -0.26±0.03 | -0.02±0.03 |

Table 2: Total number of baryons and antibaryons, within solid angle covered by detector. Results from 40 TeV simulation with $n_B$ given by the LOME estimate.
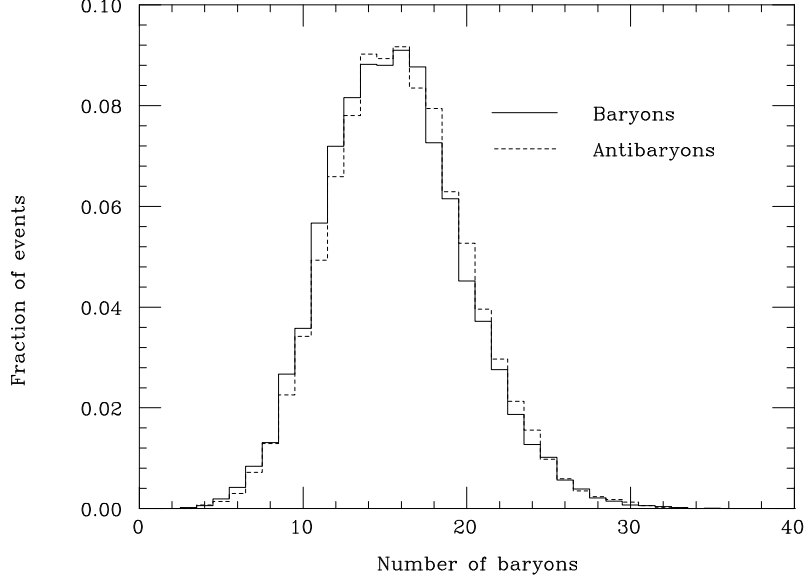


Figure 14: Number of baryons and antibaryons observed in detector per event. Solid line baryons, dotted line antibaryons.

Table 2.

In order to estimate the number of events required for baryon number violation to be established at a suitable confidence level, we compare two sets of data. The first is a mixture of BLNV and multi–W events in equal amounts, corresponding to an equal probability for these two processes. The second set of data is the multi–W process alone, and we calculate the confidence level of separating the two data sets as a function of the number of events, using Student's $t$ test [77], as described in appendix B.

This analysis predicts that approximately $8.10^3$ events are needed to verify B violation at the 95% confidence level. However, this is assuming a 100% efficiency of baryon identification, which is far from realistic. The number of events required for a given confidence level is approximately proportional to $1/\zeta^2$ for an efficiency of $\zeta$. Using a figure of 1% for this efficiency, which is probably a very generous overestimate,[8] the number of events is then $\sim 10^8$. By concentrating on types of baryons with particularly distinctive decay modes, it may be possible to decrease this figure, but it is unlikely that any reduction by orders

---

[8]We thank M.A. Parker for useful discussions on this point.

| Events passing lepton counting cuts | | | | | | |
|---|---|---|---|---|---|---|
| Energy | BLNV | | | Multi–W | | |
| TeV | Electron | Muon | Either | Electron | Muon | Either |
| 17 | 55.8 | 55.2 | 81.1 | 38.4 | 38.0 | 63.2 |
| 40    (a) | 72.5 | 70.5 | 92.8 | 51.1 | 49.7 | 77.2 |
| 40    (b) | 99.5 | 99.6 | 100.0 | 99.3 | 99.3 | 100.0 |
| 200 | 75.0 | 73.0 | 94.0 | 51.7 | 50.9 | 77.5 |

Table 3: Percentage of events passing lepton count cuts. For the 40 TeV simulations, case (a) is $n_B \sim 1/\alpha_W$, case (b) LOME prescription.

of magnitude is possible. We conclude that the verification of B violation is effectively impossible for the types of processes considered here.

## 3.3   Lepton number violation signatures

A more promising signature for BLNV is the violation of lepton number. Unlike the baryons from the primary process, which tend to be found amongst the low-momentum debris after hadronization of the excess antiquarks as discussed in Sect. 2.3, the excess leptons emerge directly from the primary process with high momenta and can be identified. It is not possible to demonstrate L violation for a single event, as it is not possible to detect the produced neutrinos. However, it may be possible to demonstrate an asymmetry by considering the average number of leptons and antileptons produced in a set of events. In this section we discuss the possibility of observing lepton number violation using both model-independent and model-dependent techniques. We restrict our discussion to $e^{\pm}$ and $\mu^{\pm}$ leptons.

Simulations performed for the four cases listed in Table 1 show that L violation is much easier to demonstrate than B violation. Therefore a more detailed analysis of the characteristics of the leptons is warranted. Recall that a cut on the minimum number of detected leptons has been imposed. In order for an event to be included in the analysis, it has to contain at least four electrons or four muons. The cut chosen is similar to those that will have to be made at the trigger level at any high luminosity supercollider. This cut also helps in some cases to reduce the multi–W background. Table 3 summarises the number of events passing this cut.

The simplest method of verifying the non-conservation of lepton number is to measure the quantity

$$D_l = N_{l^-} - N_{l^+} \tag{43}$$

and demonstrate that it is incompatible with lepton number conservation. Such a measurement can be considered model independent in the sense that it does not depend on the details of the matrix element of the hard process, provided the effect of the detector cuts at low $p_T$ and high rapidity can be neglected.

| Lepton number results | | | | |
|---|---|---|---|---|
| Energy | $D_e$ | | $D_\mu$ | |
| TeV | BLNV | Multi–W | BLNV | Multi–W |
| 17 | -0.48±0.02 | -0.09±0.02 | -0.47±0.02 | -0.07±0.02 |
| 40  (a) | -0.47±0.02 | -0.09±0.02 | -0.49±0.02 | -0.11±0.02 |
| 40  (b) | -0.47±0.03 | -0.08±0.03 | -0.45±0.03 | -0.10±0.03 |
| 200 | -0.40±0.02 | -0.04±0.02 | -0.41±0.02 | -0.10±0.02 |

Table 4: Average value of lepton number differences $D_e$ and $D_\mu$. Results based on $10^4$ event simulations.
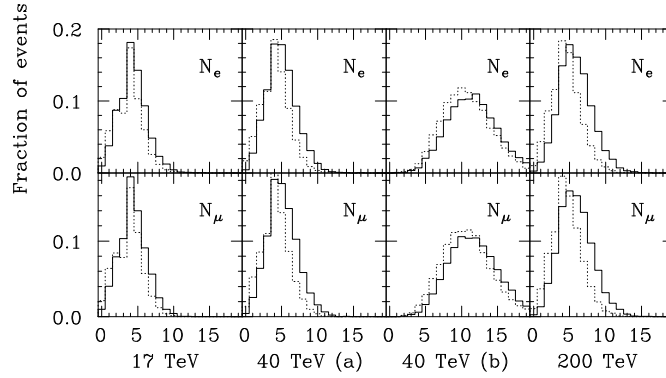


Figure 15: Total number of observed leptons per event. Solid line BLNV process, dotted L conserving multi-W process.

One antilepton of each family is produced by the instanton interaction (5). Consequently, we expect that the average of $D_l$ for a large enough number of BLNV events will tend to a value of $-0.5$ for each lepton family. However, there are a number of factors which modify this prediction. The branching ratio of a W(Z) boson to a lepton-antilepton pair is 11%(3.3%). Hence, for $n_B$ electroweak bosons the decay products will include on average $0.1n_B$ leptons of each type, with a Poisson distribution. The average incoming charge of the hard process is non-zero in both the BLNV and multi–W cases, which results in a non-zero average total charge for the outgoing bosons, and consequently a non-zero value of $D_l$ even in processes which conserve lepton number. In addition, not all the leptons will be detected, and there will also be contributions to $D_l$ from the decays of heavy quarks and antiquarks. The effect of these factors can be seen in the measured values of $D_e$ and $D_\mu$ listed in Table 4.

We first consider the general properties of the $N_{l\pm}$ and $D_l$ distributions before discussing the possibility of observing lepton number violation. The results for $N_{l-} + N_{l+}$ for both muons and electrons are plotted in Fig. 15 for each of the four simulations. The difference between the BLNV and multi–W cases can be clearly seen and is due to the extra antilepton from the primary interaction in the former case.

The number of leptons produced and detected is primarily determined by $n_B$, with the
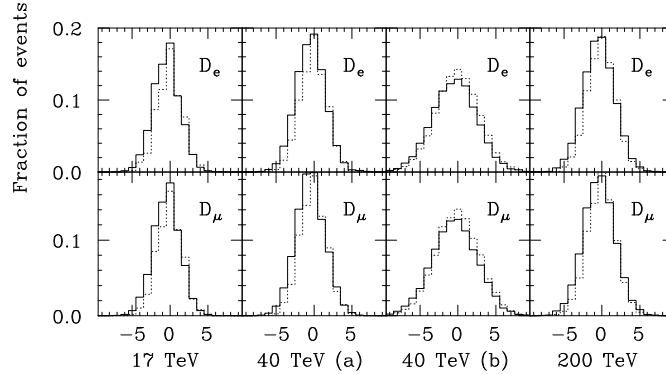
Figure 16: Difference in lepton number $D_l$ for muons and electrons. Solid line BLNV process, dotted L conserving multi-W process.

main secondary effect coming from the detector cuts and inefficiencies. The effect of the cuts depends on the 'centrality' of the interaction. If the threshold is large in comparison to the total beam energy then the interaction rest frame will tend to be nearly stationary in the detector frame. As the beam energy increases relative to the threshold, the interaction frame is more likely to be moving in the detector frame and consequently more particles are likely to be lost at high rapidity.

The lepton number differences $D_l$ for $l = e, \mu$ are plotted in Fig. 16. These plots show a similar parameter dependence to the $N_l$ plots. The antileptons from the BLNV processes cause the differences between the BLNV (solid line) and multi–W (dashed line) plots. This difference is also apparent in the average values of the distributions, shown in Table 4. In the multi–W case $\langle D_e \rangle$ and $\langle D_\mu \rangle$ are close to zero. The small non-zero values of these quantities represent the bias from starting with incoming protons, and the other factors as discussed above.

The mean differences $\langle D_l \rangle$ can be used to demonstrate the existence of L violation. In the same manner as the baryon case, the number of events required to do this is estimated by comparing an equal mixture of BLNV and multi–W events to a set of multi–W events alone. The estimates of the number of events required to be inconsistent with the multi–W data at the 95% confidence level are given in Table 5. These estimates are written in terms of the total number of events (BLNV and multi–W combined); of the order of $10^3$ events are needed to verify the existence of an asymmetry.

We shall now consider other methods for demonstrating lepton number violation. Our aim here is only to investigate techniques that might aid in the verification of lepton number violation. In particular, we consider the possibility of enhancing the BLNV event sample to improve the determination of $D_e$ and $D_\mu$ by studying the momentum distribution of the leptons, and also other indirect signatures of lepton number violation. We note that any analysis based on enhancing the sample using the momenta is dependent on the structure of the matrix element, and a quantitative analysis would require more detailed modelling of the underlying processes.

It has been pointed out in [11] that tagging events by the sign of the highest energy

| Number difference events | | |
| --- | --- | --- |
| Energy/TeV | $D_e$ | $D_\mu$ |
| 17 | 660 | 770 |
| 40 (a) | 890 | 670 |
| 40 (b) | 2700 | 2570 |
| 200 | 900 | 1250 |

Table 5: Number of events for demonstrating BLNV at a 95% confidence level by measuring lepton number differences. Case (a) at 40 TeV is $1/\alpha_W$ number of bosons, case (b) LOME prediction.

lepton should enhance the asymmetry caused by BLNV. This is because the most energetic $l^-$ in any event can only come from the decay of a gauge boson, whereas the highest energy $l^+$ could have originated from either boson decay or the primary interaction. We define the energy

$$E_{l^+} = \text{Max}\, E\left(l^+\right) \tag{44}$$

for events with

$$\text{Max}\, E\left(l^+\right) > \text{Max}\, E\left(l^-\right) \tag{45}$$

together with the corresponding $E_{l^-}$ for events where the most energetic lepton is an $l^-$. Events with no leptons of the type under consideration passing the detector cuts are discarded.

The average energy of a primary lepton from the BLNV interaction, which can only contribute to the $E_{l^+}$ distribution, is $\sim \bar{E}$, whereas a lepton from the decay of a gauge boson, which can contribute to both distributions, has an average energy $\sim (\bar{E} + m_W)/2$. Therefore the enhancement of a sample of BLNV events by selecting according to the highest energy lepton will depend on the ratio of $\bar{E}$ to $m_W$. For multi–W events, all the leptons are produced by gauge boson decay and so there is only a small difference between the $E_{l^+}$ and $E_{l^-}$ spectra due to the non-zero charge of the incoming protons.

At large $n_B$, it is permissible to make the approximation $\bar{m} \sim m_W$. This gives

$$\frac{\bar{E} + m_W}{2} \sim \frac{f_W\, m_W}{2} \tag{46}$$

whereas

$$\bar{E} \sim m_W(f_W - 1). \tag{47}$$

In the limiting case of $f_W$ close to 1, leptons from the BLNV process will have much less energy (close to zero) than those from gauge boson decay ($\sim m_W/2$). As $f_W$ is increased, this imbalance is reduced. At $f_W \sim 2$, the average kinetic energy of the BLNV leptons will be similar to that of leptons from gauge boson decay. As $f_W$ increases above this value, the BLNV leptons will tend to have higher average kinetic energies than their boson decay product counterparts. Therefore, as $f_W$ increases the difference between the $E_{l^+}$ and $E_{l^-}$ spectra will become more pronounced. Note that there will always be some asymmetry between the spectra caused by the extra antilepton from the BLNV process.
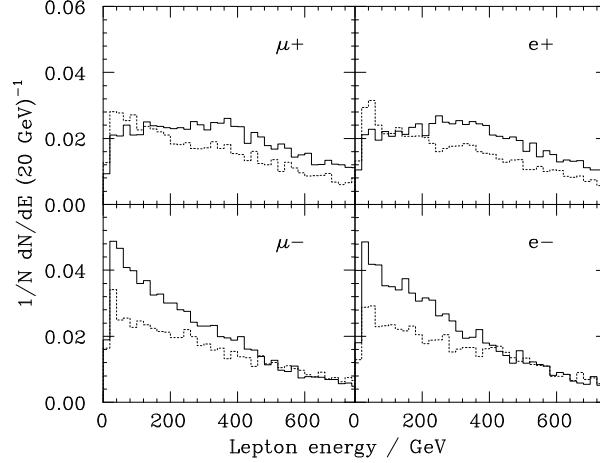
Figure 17: Highest energy lepton spectra for 40 TeV ($n_W \sim 1/\alpha_W$) simulation. In Figs. 17-20, the solid lines represent BLNV events, the dashed lines the L-conserving background.
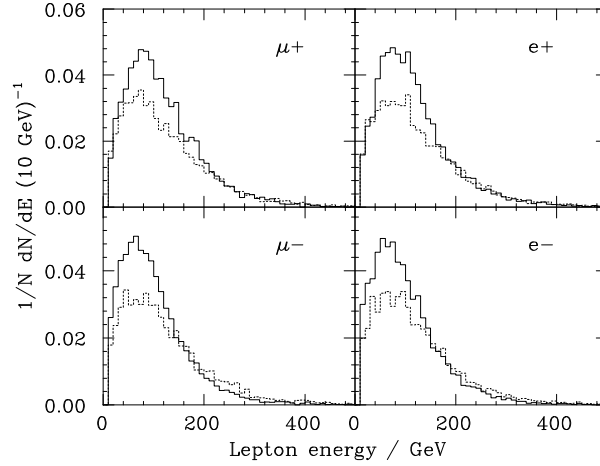


Figure 18: Highest energy lepton spectra for 40 TeV (LOME prediction for $n_B$) simulation.

Using $f_W$ to classify the simulations listed in Table 1, we can divide them into two pairs. The distributions of $E_{l+}$ and $E_{l-}$ are plotted for the two 40 TeV simulations in Figs. 17 and 18 for $f_W \sim 7.4$ ($n_B$ given by the LOME prescription) and $f_W \sim 2$ ($n_B \sim 1/\alpha_W$) respectively. The enhancement of the $E_{l+}$ spectra at large $f_W$ can be clearly seen.

The spectra of Figs. 17 and 18 have been normalised so that the total area under each curve is proportional to the number of events contributing to that distribution. By considering the relative entries to the two distributions $E_{l+}$ and $E_{l-}$, it may be possible to observe an asymmetry between the $l^+$ and $l^-$ data. As shown in Table 6, a small asymmetry is expected in the case of L conserving multi-W events, due to the initial state charge, and a much larger one in the BLNV case. The estimates for the number of events required to demonstrate an asymmetry, using the same mixing of BLNV and multi-W events as before, are shown in Table 7.

| Relative numbers of highest energy leptons | | | |
|---|---|---|---|
| Energy (TeV) | Lepton | BLNV events | Multi–W events |
| 17 | $e^+$ | 58.4 | 50.2 |
| | $e^-$ | 40.4 | 46.4 |
| | $\mu^+$ | 59.7 | 49.7 |
| | $\mu^-$ | 38.9 | 47.0 |
| 40 (a) | $e^+$ | 64.8 | 50.1 |
| | $e^-$ | 34.8 | 47.7 |
| | $\mu^+$ | 64.7 | 50.9 |
| | $\mu^-$ | 34.8 | 47.4 |
| 40 (b) | $e^+$ | 55.8 | 50.6 |
| | $e^-$ | 44.2 | 49.4 |
| | $\mu^+$ | 55.9 | 50.0 |
| | $\mu^-$ | 44.1 | 50.0 |
| 200 | $e^+$ | 63.9 | 49.7 |
| | $e^-$ | 35.6 | 48.3 |
| | $\mu^+$ | 63.7 | 50.1 |
| | $\mu^-$ | 35.7 | 48.1 |

Table 6: Relative number of entries, as percentages, of the lepton energy distributions $E_{l^+}$ and $E_{l^-}$ for $10^4$ event simulations. For the 40 TeV simulations, case (a) refers to $n_B \sim 1/\alpha_W$, case (b) LOME prescription for $n_B$.

| No. events rel. occurrence | | |
|---|---|---|
| Energy/TeV | $\mu^\pm$ | $e^\pm$ |
| 17 | 340 | 285 |
| 40 (a) | 150 | 145 |
| 40 (b) | 1130 | 1375 |
| 200 | 170 | 180 |

Table 7: Number of events for 95% confidence level by measuring relative occurrence of $l^+$ and $l^-$ as the highest energy lepton of an event, compared with the multi–W background predictions.

| Energy asymmetry | | |
| --- | --- | --- |
| Energy/TeV | Electron | Muon |
| 17 | $3.7\ 10^3$ | $1.7\ 10^4$ |
| 40 (a) | $6.0\ 10^2$ | $9.5\ 10^2$ |
| 40 (b) | $3.5\ 10^4$ | $2.2\ 10^4$ |
| 200 | $7.6\ 10^2$ | $7.1\ 10^2$ |

Table 8: Number of events for 95% confidence level by measuring asymmetry in energy of highest energy lepton by event.

| Number difference events | | | | |
| --- | --- | --- | --- | --- |
| Energy/TeV | $D_e^+$ | $D_e^-$ | $D_\mu^+$ | $D_\mu^-$ |
| 17 | $1.1\ 10^4$ | $7.5\ 10^3$ | $9.4\ 10^3$ | $1.1\ 10^4$ |
| 40 (a) | $2.0\ 10^4$ | $2.4\ 10^4$ | $9.8\ 10^3$ | $2.9\ 10^4$ |
| 40 (b) | $1.4\ 10^4$ | $1.1\ 10^4$ | $1.7\ 10^4$ | $2.0\ 10^4$ |
| 200 | $1.6\ 10^4$ | $2.5\ 10^4$ | $4.7\ 10^4$ | $4.0\ 10^4$ |

Table 9: Number of events for demonstrating BLNV at a 95% confidence level by measuring lepton number differences with samples enhanced by the sign of the highest energy lepton.

The BLNV leptons distort the shape of the $E_{l+}$ distributions compared to the $E_{l-}$ ones. Thus, another experimental test is the comparison of these spectra. Within the context of our model, we may estimate how many events are needed to see an asymmetry in the average values of these spectra, by mixing BLNV and multi–W data in the same way as before. The estimates for the number of events are given in Table 8. It should be stressed again, however, that the energy spectra are model dependent and so any attempt to verify an asymmetry based on analysing the lepton spectra would be less reliable than simple lepton counting.

With this reservation in mind, we now consider refining the lepton counting technique. We define two distributions, $D_l^+$ and $D_l^-$, by separating the measurement of $D_l$ according to the sign of the highest energy lepton ($l^+$ or $l^-$) on an event-by-event basis. These distributions are plotted in Fig. 19 for the muons and Fig. 20 for the electrons. The corresponding average values of $D_l^+$ and $D_l^-$ for the multi–W case are also non-zero, due mainly to the bias introduced by using the lepton charge sign for event selection. The averages of these distributions can be used as a signature of L violation, and estimates of the number of events required are shown in Table 9. Note that these estimates refer to the *total* number of events. Despite the enhancement of the signal due to the cut on the lepton charge, the total number of events required is comparable to working with $D_l$ alone, due to the fact that we have a reduced sample size.

Some comments on the experimental considerations of detecting leptons are in order. The large number of particles present in the detector as a result of a BLNV process will make the identification of the particles difficult. As discussed in Sect. 2.4, there is little
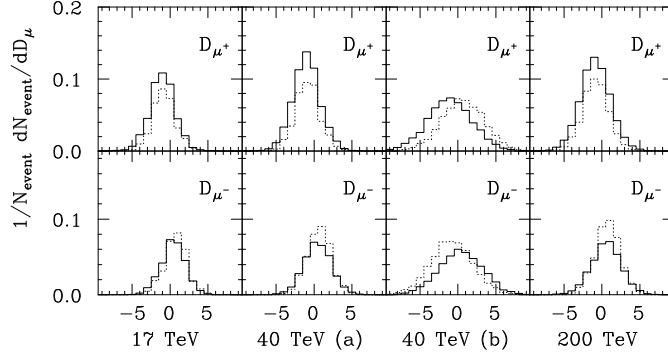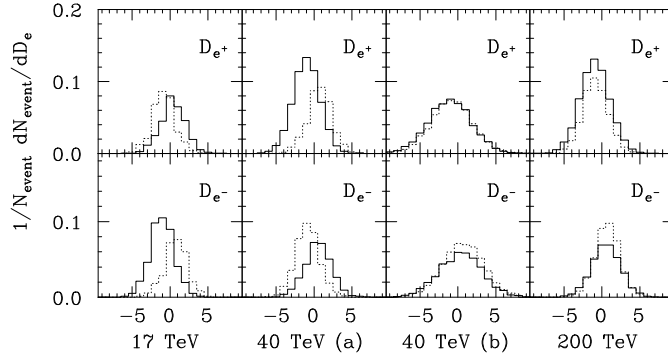
Figure 19: Difference in muon number.



Figure 20: Difference in electron number.

chance of identifying individual jets or reconstructing the bosons from the underlying hard process. However, it may be possible to reconstruct leptonic $Z^0$ decays. This would reduce the number of leptons in the $D_l$ analyses, and therefore should decrease the size of the fluctuations. In addition, the $Z^0$ momentum spectrum could then be obtained from the reconstruction process. However, a more detailed simulation of the measurement of lepton energy and momentum is required to investigate this further.

The detection criteria used are very simplistic, and any attempt to detect BLNV experimentally would require a more complete detector simulation. In particular, the isolation of electrons is complicated by the presence of many nearby particles, which may 'fake' an electron in the detector. On the other hand, muons are normally identified at the outer edge of a detector after having passed through the intervening material. Therefore, muon identification will probably be easier than electron identification.

It may be possible to alleviate some of the detection problems by considering only isolated leptons. Repeating the analysis based upon $D_e$ and $D_\mu$ for the 40 TeV (LOME prescription for $n_B$) simulation leads to an estimate of $\sim 10^4$ events for a 95% confidence level in verifying L violation. The larger number of events required is due to the rejection of the non-isolated leptons, which amount to approximately 80%, reducing the statistics

considerably. The other three simulations, being based on a $n_B \sim 1/\alpha_W$ approximation, have on average less leptons per event; this is offset by the fact that there are fewer particles in the detector. In order to investigate isolated leptons further, a more detailed study, ideally including a full detector simulation, is required.

# 4    Conclusions

We have discussed the construction, implementation and study of a phenomenological model for BLNV processes. The characteristic boson multiplicities and energies which are a feature of calculations based upon instanton and sphaleron processes within the Standard Model have been incorporated.

The high boson multiplicities mean that such processes are very distinctive from an experimental point of view. Particular characteristics of the processes are their high threshold energy, leading to 'central' events in the detector, the spherical nature of the interactions, and the high particle multiplicities. The high transverse energy of the final state, combined with the large number of high $p_T$ leptons and the inability to resolve jets means that any conventional Standard Model background can be easily separated. We have argued that the only significant background is that of non-perturbative multi-W(Z) production, with typical boson multiplicities $\sim 1/\alpha_W$.

In our calculations we have taken into account the breaking of the electroweak symmetry. We expect that the approximate ratio of outgoing final state bosons in the BLNV process is $1 : 1 : \cos^2\theta_W : \sin^2\theta_W$ for the $W^+$, $W^-$, $Z^0$ and $\gamma$ particles respectively. This has allowed the study of the production of photons in BLNV interactions for the first time. The high energy and high $p_T$ regions of the photon spectra are dominated by these photons, indicating that the boson distributions from the BLNV matrix elements can be directly studied. This study can be enhanced by including reconstruction of leptonic $Z^0$ decays if possible.

The studies described here confirm that the demonstration of baryon number violation is effectively impossible. The 'extra' antibaryons from the B violating vertex are in general produced at low energy and $p_T$, which makes them difficult to isolate from the large number of other hadrons produced. In addition, the charge of a baryon or antibaryon is not directly related to the baryon number of the particle. There is also the added problem of the low efficiency of baryon identification at a supercollider. We quantify our pessimistic conclusion by estimating the number of BLNV (and multi-W background) events required to verify B violation as at least $10^8$.

On the other hand, the studies show that the verification of lepton number violation is possible, provided that the cross section of the BLNV process is high enough. Charged leptons are relatively easy to identify at a supercollider, and there is the advantage that the lepton number of a charged lepton is proportional to its charge. A simple model independent test of L violation is to count the number of $l^+$ and $l^-$ produced on an event-by-event basis, and demonstrate an incompatability with L conservation. We find that $\sim 10^3$ events would be required.

We have also considered the enhancement of the sample of BLNV events compared to the background. In particular, the momentum distribution of the antileptons from the BLNV process differs from that of the leptonic decay products of the other outgoing particles. Our studies show that using this difference, in general, reduces the number of events one needs to demonstrate an asymmetry, to $\sim 10^2$ events. It must be stressed, however, that any enhancement of the sample using this requires some knowledge of the momentum distribution of the outgoing particles from the BLNV interaction. Therefore, any such study is not model independent.

The predictions made from these studies can be improved in a number of ways. The most obvious is to improve the understanding of the momentum distribution and angular structure of the outgoing state. Calculation of these quantities for the instanton matrix element (or any similar non-perturbative process with a high boson multiplicity) is at present not possible due to the large number of terms. Some insight may be gained by the type of approach used to study sphaleron decays, which we saw are similar to our model predictions in the corresponding region of parameter space.

We close with some comments on the future prospects for studying not only BLNV but non-perturbative processes in general. One possibility is the observation of multi-W processes in cosmic ray interactions [78, 79]. In particular, constraints can be placed on the cross section for such processes in advance of any supercollider study. Secondly, there is theoretical evidence [80, 81] that instanton processes in QCD may be observed in deep inelastic $ep$ scattering at HERA [82].

# Appendix A - The HERBVI event generator

The HERBVI event generator [12] is a package written as an extension to the Monte Carlo program HERWIG, and is based on the MAMBO [54] event generation algorithm. Versions of HERWIG from 5.7 onwards contain hooks to allow the use of this package. The interface to HERWIG consists of four routines:

**HVINIT** Initialization routine. This sets up the physical parameters for the simulation. Once it has been called, the user can modify these parameters. If it has not been called before the first call to `HVHBVI`, it is executed then.

**HVCBVI** Clustering routine. This is executed within HERWIG to enable the antiquarks produced in the baryon number violating process to be joined up according to the colour constraints described in Sect. 2.3.

**HVHBVI** Main event generator, called by HERWIG for process codes `IPROC` 7000 to 7999. At present, two processes are generated by this routine,
   7000   BLNV event generation
   7100   Multi–W event generation

**HVANAL** Initial event analysis. This routine produces a table of all final state particles and a flag to indicate if the particle is from the initial BLNV interaction. The rapidity and transverse momentum of each final state particle is calculated.

In addition, provision has been made for user generation of both the parton-level cross section and the boson number distribution. The routines `HUSGEN` (parton-level cross section) and `HURBOS` (boson number distribution) are called if the appropriate flags (`HUFSFG` and `HUFRBN` respectively) are set `TRUE`.

Final-state particle momenta are generated using the MAMBO algorithm, and to each event a weight $w$ is assigned. The HERWIG package produces an unweighted distribution by accepting events for which the ratio $w/w_{max}$ exceeds a random number between 0 and 1. The maximum weight $w_{max}$ is determined by a search at the start of the simulation.

In order to generate events with a high efficiency, two simplifications are made. Firstly, for each event only a *relative* weight is calculated. This removes the need to calculate the phase space integral for a given configuration. This integral is constant for a fixed boson multiplicity, and the relative weight for different $n_B$ is taken into account when the boson multiplicity distribution is generated. Secondly, events are generated isotropically, as discussed above. These two steps reduce the 'tails' of the weight distribution, and consequently increase the efficiency of the Monte Carlo. It is straightforward to include the effect of a non-trivial matrix element by reweighting the events generated by HERBVI. However, this will decrease the efficiency.

Use of the HERBVI package requires that the dummy routines `HVCBVI` and `HVHBVI` be deleted from the HERWIG package, and that both programs are compiled with larger common blocks. We find that a 10000 event simulation takes approximately 5 to 10 hours to run on a Vax4000 workstation. About a third of this time is used by HERBVI when generating events. More details of the HERBVI package are available from the authors, who can be contacted by electronic mail at `gibbs@cbhep.cern.ch` and `webber@vxcern.cern.ch`.

# Appendix B - The Student's t test

The Student's $t$ test is a standard tool in statistical analysis for estimating the significance of a particular set of measurements, or that of the difference between two sets of measurements. Let $\bar{x}_1$ and $\bar{x}_2$, with variances $\sigma_1^2$ and $\sigma_2^2$, be the result of two sets of measurements with $n_1$ and $n_2$ points in each set respectively. We define the combined variance as

$$\sigma_t^2 = \left(\frac{\sigma_1^2}{n_2} + \frac{\sigma_2^2}{n_1}\right)\frac{n_1 + n_2}{n_1 + n_2 - 2} \tag{48}$$

with the number of degrees of freedom

$$N = n_1 + n_2 - 2. \tag{49}$$

The estimate of the significance is then performed by using the Student's $t$ distribution by evaluating

$$t = \frac{\bar{x}_1 - \bar{x}_2}{\sigma_t} \tag{50}$$

and computing the confidence level

$$F(t, N) = \frac{\Gamma\left(\frac{1}{2}(N+1)\right)}{\sqrt{\pi N}\Gamma\left(\frac{1}{2}\right)} \int_{-\infty}^{t} \left(1 + \frac{x^2}{N}\right)^{-\frac{1}{2}(N+1)} \mathrm{dx}. \tag{51}$$

F is then an estimate of the statistical significance of the difference between the two sets of measurements. A fuller discussion of this test is given in [77].

# Referencesmkboth REFERENCESREFERENCES

[1] A. Ringwald, Nucl. Phys. B330 (1990) 1.

[2] O. Espinosa, Nucl. Phys. B343 (1990) 310.

[3] L. McLerran, A. Vainshtein and M. Voloshin, Phys. Rev. D42 (1990) 171.

[4] J. Cornwall, Phys. Lett. B243 (1990) 271.

[5] H. Goldberg, Phys. Lett. B246 (1990) 445.

[6] H. Goldberg, Phys. Rev. D45 (1992) 2945.

[7] M. Mattis, Phys. Rev. 214 (1992) 159.

[8] P. Tinyakov, Int.J.Mod.Phys. A8 (1993) 1823.

[9] A. Ringwald, CERN preprint CERN-TH.6862 (1993).

[10] A. Ringwald, F. Schrempp and C. Wetterich, Nucl. Phys. B365 (1991) 3.

[11] G. Farrar and R. Meng, Phys. Rev. Lett. 65 (1990) 3377.

[12] M.J. Gibbs and B.R. Webber, in preparation.

[13] S. Adler, Phys. Rev. 177 (1969) 2426.

[14] J. Bell and R. Jackiw, Nuovo Cimento 51 (1969) 47.

[15] W.A. Bardeen, Phys. Rev. 185 (1969) 1848.

[16] G. 't Hooft, Phys. Rev. D14 (1976) 3432.

[17] G. 't Hooft, Phys. Rev. Lett. 37 (1976) 8.

[18] R. Jackiw and C. Rebbi, Phys. Rev. Lett. 37 (1976) 172.

[19] C. Callan, R. Dashen and D. Gross, Phys. Lett. B63 (1976) 334.

[20] N. Manton, Phys. Rev. D28 (1983) 2019.

[21] F. Klinkhammer and N. Manton, Phys. Rev. D30 (1984) 2212.

[22] L. Yaffe, in: Proc. of the Santa Fe Workshop on Baryon Number Violation at the SSC?, eds. M. Mattis and E. Mottola. (World Scientific, Singapore, 1990).

[23] P. Arnold and M. Mattis, Phys. Rev. D42 (1990) 1738.

[24] S. Khlebnikov, V. Rubakov and P. Tinyakov, Nucl. Phys. B350 (1991) 441.

[25] A.H. Mueller, Nucl. Phys. B348 (1991) 310.

[26] A.H. Mueller, Nucl. Phys. B353 (1991) 44.

[27] M. Voloshin, Nucl. Phys. B359 (1991) 301.

[28] V. Zakharov, Minnesota preprint TPI-MINN-90/7-T (1990).

[29] M. Porrati, Nucl. Phys. B347 (1990) 371.

[30] V.V. Khoze and A. Ringwald, Nucl. Phys. B355 (1991) 351.

[31] D. Diakonov and V. Petrov, in: Proc. of the 26th Winter School of the Leningrad Nuclear Physics Institute (1991).

[32] A.H. Mueller, Nucl. Phys. B364 (1991) 109.

[33] P. Arnold and M. Mattis, Mod. Phys. Lett. A6 (1991) 2059.

[34] D. Diakonov and M. Polyakov, St. Petersburg preprint LNPI-1737 (1991).

[35] I. Balitskii and A. Schäfer, Nucl. Phys. B404 (1993) 639.

[36] P.G. Silvestrov, Phys. Lett. B323 (1994) 25.

[37] V. Zakharov, Nucl. Phys. B371 (1992) 637.

[38] V.I. Zakharov, Nucl. Phys. B353 (1991) 683.

[39] M. Maggiore and M. Shifman, Nucl. Phys. B365 (1991) 161.

[40] G. Veneziano, Mod. Phys. Lett. A7 (1992) 1661.

[41] H. Aoyama and H. Goldberg, Phys. Lett. B188 (1987) 506.

[42] P. Arnold and L. McLerran, Phys. Rev. D37 (1988) 1020.

[43] M. Hellmund and J. Kripfganz, Nucl. Phys. B373 (1992) 749.

[44] J. Zadrozny, Phys. Lett. B284 (1992) 88.

[45] B. Ratra and L.G. Yaffe, Phys. Lett. B205 (1988) 258.

[46] E. Witten, Phys. Rev. Lett. 38 (1977) 121.

[47] N. Turok and J. Zadrozny, Nucl. Phys. B358 (1991) 471.

[48] T. Akiba, H. Kikuchi, and T. Yanagida, Phys. Rev. D40 (1989) 588.

[49] J.R. Klauder and E.C.G. Sundarshan, *Fundamentals of Quantum Optics.* Benjamin, New York, 1968.

[50] W.-M. Zhang, D.H. Feng, and R. Gilmore, Rev. Mod. Phys. **62** (1990) 867.

[51] C. Itzykson and J. Zuber, *Quantum Field Theory.* McGraw Hill, 1985.

[52] E. Eichten, I. Hinchliffe, K. Lane and C. Quigg, Rev. Mod. Phys. 58 (1986) 1065.

[53] E. Bykling and K. Kajantie, *Particle Kinematics* , Wiley-Interscience Pub., 1971.

[54] R. Kleiss and J. Stirling, Nucl. Phys. B385 (1992), 413.

[55] W. J. Stirling, R. Kleiss and S. D. Ellis, Comp. Phys. Comm. 40 (1986) 359.

[56] M.J. Gibbs, A. Ringwald and B.R. Webber, in preparation.

[57] G. Marchesini, B.R. Webber, G. Abbiendi, I.G. Knowles, M.H. Seymour and L. Stanco, Comp. Phys. Comm. 67 (1992) 465.

[58] G. Marchesini and B.R. Webber , Nucl. Phys. B310 (1988) 461.

[59] T. Sjöstrand, Comp. Phys. Comm. 39 (1986) 347.

[60] M. Bengtsson and T. Sjöstrand, Comp. Phys. Comm. 43 (1987) 367.

[61] B.R. Webber, Nucl. Phys. B238 (1984) 492.

[62] B. Andersson, G. Gustafson, G. Ingelman and T. Sjöstrand, Phys. Rep. 97 (1983) 33.

[63] A.H. Mueller, Phys. Lett. 104 (1981) 161.

[64] B.I. Ermolaev and V.S. Fadin, JETP Lett. 33 (1981) 285.

[65] Yu.L. Dokshitzer, V.A. Khoze, A.H. Mueller and S.I. Troyan, *Basics of Perturbative QCD*, Editions Frontieres, 1991.

[66] G. Marchesini and B.R. Webber, Nucl. Phys. B238 (1984) 1.

[67] G. Marchesini and B.R. Webber, Nucl. Phys. B330 (1990) 261.

[68] V. Barger, A.L. Stange and R.J.N. Phillips, Phys. Rev. D45 (1992) 1484.

[69] D.A. Morris, Talk at *Workshop on Physics at Current Accelerators and the Supercollider*, UCLA preprint 93/TEP/30.

[70] W.T. Giele, T. Matsuura, M.H. Seymour and B.R. Webber, in *Research Directions for the Decade*, Proc. 1990 Snowmass Summer Study on High Energy Physics, ed. E.L. Berger (World Scientific, Singapore, 1992).

[71] F.A. Berends, H. Kuijf, B. Tausk and W.T. Giele, Nucl. Phys. B357 (1991) 32.

[72] R.S. Chivukula, M. Golden and E.H. Simmons, Nucl. Phys. B363 (1991) 83.

[73] R. Odorico, Int. J. Mod. Phys. A5 (1990) 3617.

[74] H. Goldberg and R. Rosenfeld, Northeastern University preprint NUB-3061/93-Th. (1993).

[75] ATLAS collaboration, *Letter of Intent*, CERN/LHCC/92-4.

[76] CMS collaboration, *Letter of Intent*, CERN/LHCC/92-3.

[77] W.H. Press, S.A. Teukolsky, W.T. Vetterling and B.P. Flannery, *Numerical Recipes in FORTRAN, Second Edition*, Cambridge Univ. Press, 1992.

[78] D.A. Morris and R. Rosenfeld, Phys. Rev. D44 (1991) 3530.

[79] D.A. Morris and A. Ringwald, Astroparticle Physics 2 (1994) 43.

[80] V.V. Khoze and A. Ringwald, Phys. Let. B259 (1991) 106.

[81] I.I. Balitsky and V.M. Braun, Phys. Lett. B314 (1993) 237.

[82] I.I. Balitsky and V.M. Braun, Phys. Rev. D47 (1993) 1879.

This figure "fig1-1.png" is available in "png" format from:

http://arXiv.org/ps/hep-ph/9406266v1

This figure "fig2-1.png" is available in "png" format from:

http://arXiv.org/ps/hep-ph/9406266v1

This figure "fig3-1.png" is available in "png" format from:

http://arXiv.org/ps/hep-ph/9406266v1

This figure "fig1-2.png" is available in "png" format from:

http://arXiv.org/ps/hep-ph/9406266v1

This figure "fig2-2.png" is available in "png" format from:

http://arXiv.org/ps/hep-ph/9406266v1

This figure "fig3-2.png" is available in "png" format from:

http://arXiv.org/ps/hep-ph/9406266v1

This figure "fig1-3.png" is available in "png" format from:

http://arXiv.org/ps/hep-ph/9406266v1

This figure "fig2-3.png" is available in "png" format from:

http://arXiv.org/ps/hep-ph/9406266v1

This figure "fig3-3.png" is available in "png" format from:

http://arXiv.org/ps/hep-ph/9406266v1

This figure "fig1-4.png" is available in "png" format from:

http://arXiv.org/ps/hep-ph/9406266v1